

Traveling spatially localized convective structures in an inclined porous medium

Zhiwei Dave Li,^{1,*} Chang Liu,^{2,†} Adrian van Kan,^{3,‡} and Edgar Knobloch^{3,§}

¹*Department of Physics, University of Washington, Seattle, WA 98195, USA*

²*School of Mechanical, Aerospace, and Manufacturing Engineering,
University of Connecticut, Storrs, CT 06269, USA*

³*Department of Physics, University of California at Berkeley, Berkeley, CA 94720, USA*

(Dated: February 18, 2025)

The coexistence of multiple stationary, spatially localized structures has recently been reported for convection in an inclined porous layer, but the influence of imperfectly conducting boundaries has not been studied. This paper analyzes the traveling behavior of asymmetric, spatially localized convective structures (‘convectons’), consisting of one or more pulses, in a two-dimensional inclined layer of a porous medium subject to a fixed temperature at the bottom and an imperfectly conducting boundary at the top, such that midplane reflection symmetry is broken. Extensive direct numerical simulations (DNS) are conducted for a wide range of Biot numbers associated with the upper boundary, revealing nontrivial relationships between the drift velocity c of spatially localized structures and the symmetry-breaking parameter $\kappa \geq 0$ based on the Biot number, with $\kappa = 0$ corresponding to perfect midplane reflection symmetry associated with $c = 0$. In small domains, the drift velocity c is positive (corresponding to upslope motion) and increases monotonically with κ , while for localized structures in larger domains consisting of a small number of pulses c can be of either sign depending on parameters. For longer structures c reverts to positive values and again increases monotonically with κ . We show that the along-slope tails of pulses and the associated long-range interactions are governed by the dominant spatial eigenvalues, whose real part is of the smallest magnitude, and uncover a transition at a finite symmetry-breaking strength $\kappa = \kappa_c > 0$: for $\kappa < \kappa_c$, both dominant eigenvalues are complex, implying that the upslope and downslope exponential tails are oscillatory. In contrast, for $\kappa > \kappa_c$, the dominant spatial eigenvalue with a positive real part becomes real, implying that the downslope exponential tail transitions from an oscillatory profile to a monotonic one. As a result, for $\kappa < \kappa_c$, bound states consisting of different numbers of pulses are present. These display rich dynamical phenomena including inelastic collisions leading to other bound states, while for $\kappa \gg \kappa_c$, adjacent pulses are found to repel one another and so tend to spread out, eventually becoming equispaced in the finite computational domain. The strength of the repulsive interaction increases with κ , i.e., with increased symmetry breaking. A reduced description of this behavior is proposed based on the interaction between tails of adjacent localized structures, which accurately reproduces the repulsion and inelastic collisions observed in DNS. The reduced model indicates that the transition from bound states to an equidistant configuration occurs when the monotonic tail and the oscillatory tail have the same slope, which occurs at a value of κ greater than κ_c . The results presented here represent a first step towards understanding the dynamics of spatially localized patterns in moderate-Rayleigh number convection in an inclined porous medium subject to an imperfectly conducting boundary.

I. INTRODUCTION

Motivated by geophysical and hydrological applications, convection in porous media has been widely studied to analyze carbon dioxide sequestration in saline aquifers [1, 2], patterned ground formation [3], the origin of polygonally shaped crusts on salt lakes [4], and the melting of ice [5]. Moreover, the applications of fluid flow in porous media extend beyond geophysics to biomechanics and chemical and mechanical engineering, among others [6]. The study of convection in porous media based on Darcy’s law is also known as the Bénard–Darcy problem, a problem extensively investigated using linear stability analysis [7, 8], bifurcation analysis [9–12], and direct numerical simulations in the fully-developed turbulent regime [13–18]; see the reviews [19–22] and the textbook [23] on porous medium convection.

Studies of porous medium convection have evolved from the original setup investigated since the 1940s to incorporate additional effects like anisotropy [24–26], double diffusion [9–11, 27–29], and rotation [30], among others. One simple but practically relevant modification, in the context of geological and engineering applications, is to consider porous layers that are inclined with respect to the horizontal. The inclination of the layer leads to a background shear

* zwli@uw.edu

† chang_liu@uconn.edu

‡ avankan@berkeley.edu

§ knobloch@berkeley.edu

flow, which can significantly modify the convective instability [31–35]. Experimental and numerical studies have revealed the existence of three distinct flow regimes near the onset of convection in an inclined porous layer: a stable unicellular flow regime and two additional regimes characterized by the presence of polyhedral cells and helicoidal cells, respectively [36, 37]. These studies also examined the transitions between the different flow regimes encountered as the Rayleigh number Ra and the inclination angle ϕ are varied. Caltagirone and Bories [37] first demonstrated that the laminar base state is linearly stable for $Ra \cos \phi \leq 4\pi^2$. In a more recent numerical investigation, Rees and Bassom [38] suggested that a small angle ϕ can lead to linear instability in a two-dimensional inclined porous layer at large Ra , while at a large ϕ the base state is linearly stable and the system does not exhibit convection. Subsequent work by Wen and Chini [31] showed that in domains with large aspect ratio the base state is not energy-stable for any angle $0 \leq \phi \leq 90^\circ$ at $Ra > 91.6$, with sufficiently large disturbances yielding distinct forms of convective flows, including stable, stationary, spatially localized convection patterns with various numbers of roll pairs (or ‘pulses’) [32].

Spatially localized structures have been found in a wide range of physical systems, both conservative and dissipative [39, 40]. Knobloch [40] provides a review of spatially localized structures in different dissipative systems, starting with the Swift-Hohenberg equation [41–43] and its relatives, which provide an order-parameter description of the dynamics in many cases, extending the discussion to more complex systems including granular dynamics and fluid flows, among others. For example, spatially localized structures are widely observed in subcritical regimes of wall-bounded shear flows [44], and play an important role in the transition to turbulence; see the reviews [45, 46].

Moreover, spatially localized structures are also widely observed in convectively driven fluid flows and come in different forms. A common type of localized structure found in convective systems is the modulated traveling wave, consisting of a traveling wave state propagating with phase speed c_p under an envelope that is itself moving with a distinct group speed c_g . As a result, such states are quasi-periodic; their existence is related to the traveling waves created in a Hopf bifurcation from the conduction state. Such modulated traveling waves have been extensively studied in the context of binary fluid convection, in both experimental [47–49] and numerical settings [50–53], and collisions between them have also been investigated [54–56]. Rather than modulated traveling waves, we investigate here traveling localized states that are stationary in a comoving frame, also known as *convectons*, a term first coined in the context of magnetoconvection [57]. In contrast with modulated traveling waves, convectons are born in a steady-state secondary bifurcation from lower branch unstable spatially periodic states due to a subcritical bifurcation from the base state. In general, convectons remain stationary if they are left-right symmetric. Traveling motion of convectons therefore requires a broken reflection symmetry in the system, which may be the midplane reflection symmetry, i.e., the Boussinesq symmetry. This is physically different from the case of modulated traveling wave packets, which move because of a non-zero group speed. Convectons (both traveling and stationary) have not only been studied extensively in magnetoconvection [57–60], but also in binary fluid convection, [61–68], including in a porous medium [69] and with surface tension effects [70], and have also been seen in rotating convection [71] and in double-diffusive convection [72–75]. The transition of a steady state into a traveling one as a result of forced symmetry breaking is widely observed in pattern-forming systems [76–79]. In the work by Wen and Chini on inclined porous medium convection [32], fixed temperature boundary conditions were applied at the top and the bottom surfaces, preserving the midplane reflection symmetry and resulting in stationary localized convective structures. In practice, however, it is also physically relevant to consider imperfectly conducting boundary conditions which may lead to symmetry breaking and hence drifting motion.

In this work, we investigate the traveling behavior of convectons generated by the breaking of midplane reflection symmetry due to differing temperature boundary conditions at the top and bottom boundaries. We start by reproducing the stationary, spatially localized structures, consisting of between one and five pulses, previously found at the moderate Rayleigh number $Ra = 100$, for an inclination angle $\phi = 35^\circ$ in domains with aspect ratio $L_x = 10$ and fixed temperature at both top and bottom boundaries [32]. We use these spatially localized structures to initialize direct numerical simulations (DNS) with asymmetric boundary conditions, with fixed temperature at the bottom boundary and an imperfectly conducting top boundary. Traveling spatially localized structures are analyzed using DNS with varying symmetry-breaking strength and varying computational domains of aspect ratios $L_x \in [10, 160]$. Different initial conditions are also considered, including multiple n -pulse ($n = 1, 2, 3, 4, 5$) structures within a single domain, leading to collisions and other nontrivial behavior.

The remainder of this paper is structured as follows. In the following section, we describe the problem formulation, as well as the numerical method and relevant control parameters. In Sec. III, we focus on the dynamics of traveling spatially localized structures with one to five pulses, analyzing the relationship between the drift velocity of these structures and a symmetry-breaking parameter. We also demonstrate using DNS that the finite size of the computational domain has a significant impact on the dynamics and specifically on the stability properties of localized states. In Sec. IV, we introduce spatial eigenvalues to predict the growth/decay rate and wavelength of upslope and downslope tails of these spatially localized structures. These theoretical predictions match the results obtained through DNS and successfully predict the transition from oscillatory to monotonic tails, providing clues to the formation of

traveling bound states and the interactions between the localized structures in this system. In Sec. V, we analyze the long-time temporal dynamics of interacting localized structures. We show that when the midplane reflection symmetry is strongly broken, there is a repulsive interaction between pulses whose strength increases with the degree of symmetry breaking. In contrast, at weak symmetry breaking, stable traveling bound states consisting of n pulses exist, which propagate at different drift velocities for different n . This leads to nontrivial collision behavior, including the formation of larger stable bound states and a Newton's cradle-like phenomenon near the onset of repulsion, where a larger structure splits into smaller substructures which subsequently collide in the periodic domain, reproducing the initial structure and leading to a cyclic repetition. In Sec. VI we shed light on aspects of this behavior via a reduced description of the interaction between adjacent localized structures and show that much of the observed behavior is due to the interaction between the trailing tail of the leading structure and the leading tail of the trailing structure. The paper concludes in Sec. VII with a discussion of future directions.

II. PROBLEM FORMULATION AND NUMERICAL METHOD

A. Formulation and control parameters

We consider two-dimensional (2D) convection in an inclined porous layer with aspect ratio L_x heated from below and cooled from above as shown in Fig. 1. The system can be described by the following non-dimensional Darcy–Oberbeck–Boussinesq equations [23] in terms of velocity \mathbf{u}_{tot} , temperature T_{tot} and pressure p_{tot} :

$$\mathbf{u}_{tot} + \nabla p_{tot} = Ra T_{tot} (\sin \phi \mathbf{e}_x + \cos \phi \mathbf{e}_z), \quad (1a)$$

$$\nabla \cdot \mathbf{u}_{tot} = 0, \quad (1b)$$

$$\partial_t T_{tot} + \mathbf{u}_{tot} \cdot \nabla T_{tot} = \nabla^2 T_{tot}, \quad (1c)$$

where \mathbf{e}_x and \mathbf{e}_z are unit vectors in the x (wall-parallel) and z (wall-normal) directions, respectively. We measure lengths in units of the layer height H and time in units of the diffusive time $t_D = H^2/D$, where D is the thermal diffusivity. The velocity is normalized by $H/t_D = D/H$, and the temperature by the background temperature difference ΔT across the layer. There are three dimensionless control parameters in the problem: the inclination angle ϕ of the layer with respect to the horizontal, the domain aspect ratio $L_x \equiv L/H$ and the Rayleigh number

$$Ra \equiv \frac{\alpha g \Delta T K H}{\nu D}, \quad (2)$$

where α is the thermal expansion coefficient, g is the magnitude of gravitational acceleration, K is the Darcy permeability coefficient, and ν is the kinematic viscosity.

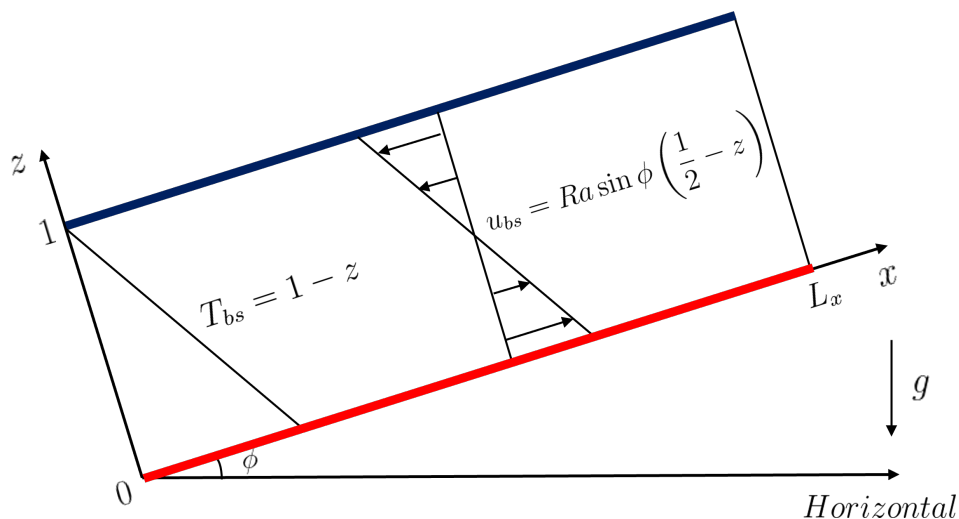


FIG. 1. Setup and dimensionless base state for 2D convection in a porous Rayleigh–Bénard cell inclined at an angle ϕ to the horizontal. The domain is taken to be periodic in the wall-parallel (x) direction. The layer is heated from below ($z = 0$) and cooled from above ($z = 1$). The base state temperature is $T_{bs} = 1 - z$ with background shear $\mathbf{u}_{bs} = u_{bs} \mathbf{e}_x = Ra \sin \phi (\frac{1}{2} - z) \mathbf{e}_x$.

The inclination of the layer generates a unidirectional shear flow, corresponding to the base state $T_{bs} = 1 - z$, $\mathbf{u}_{bs} = Ra \sin \phi \left(\frac{1}{2} - z\right) \mathbf{e}_x$, and $p_{bs} = \frac{1}{2}Ra \sin \phi x + Ra \cos \phi \left(z - \frac{1}{2}z^2\right)$, as shown schematically in Fig. 1. Decomposing T_{tot} , \mathbf{u}_{tot} , and p_{tot} into the base state and deviations from it, we have

$$T_{tot} = T_{bs} + T = 1 - z + T, \quad (3a)$$

$$\mathbf{u}_{tot} = \mathbf{u}_{bs} + \mathbf{u} = Ra \sin \phi \left(\frac{1}{2} - z\right) \mathbf{e}_x + \mathbf{u}, \quad (3b)$$

$$p_{tot} = p_{bs} + p = \frac{1}{2}Ra \sin \phi x + Ra \cos \phi \left(z - \frac{1}{2}z^2\right) + p. \quad (3c)$$

We can then write the governing equations in terms of the deviation velocity \mathbf{u} , temperature T , and pressure p :

$$\mathbf{u} + \nabla p - Ra T (\sin \phi \mathbf{e}_x + \cos \phi \mathbf{e}_z) = 0, \quad (4a)$$

$$\nabla \cdot \mathbf{u} = 0, \quad (4b)$$

$$\partial_t T + Ra \sin \phi \left(\frac{1}{2} - z\right) \partial_x T - w + \mathbf{u} \cdot \nabla T = \nabla^2 T, \quad (4c)$$

where w is the wall-normal component of the velocity perturbation \mathbf{u} . We apply periodic boundary conditions in the x direction for all variables. For boundary conditions in z , we assume impenetrability,

$$w(z=0) = w(z=1) = 0, \quad (5)$$

and impose a Dirichlet boundary condition on the temperature *deviation* T at the bottom ($z=0$) and a Robin boundary condition (Newton's law of cooling) at the top ($z=1$),

$$T(z=0) = 0, \quad (6a)$$

$$(1 - \kappa)T(z=1) + \kappa \partial_z T(z=1) = 0. \quad (6b)$$

Here, a symmetry-breaking parameter $\kappa \in [0, 1]$ is introduced in the boundary conditions, controlling the breaking of midplane reflection symmetry in terms of the upper temperature boundary condition. We note that the Biot number associated with the upper boundary is given by $(1 - \kappa)/\kappa$ and lies in $[0, \infty)$, see e.g. Chapter 6 of [23]. At $\kappa = 0$, the system is subject to symmetric Dirichlet boundary conditions (i.e., $T(z=0) = T(z=1) = 0$), leading to symmetry of the problem with respect to (diagonal) reflection $\mathcal{R} : (x, z) \rightarrow (-x, 1 - z)$, $(u, w, T) \rightarrow -(u, w, T)$.

When $\kappa = 0$ and the inclination ϕ exceeds 31.3° the base state is linearly stable for all values of Ra [32]. However, for sufficiently large Ra stable stationary \mathcal{R} -symmetric spatially localized structures can be generated by suitable finite amplitude perturbations, and these therefore coexist with the stable base state. In the present work we follow [32] and fix the inclination at $\phi = 35^\circ$ and the Rayleigh number at $Ra = 100$, focusing on the effects of breaking the reflection symmetry \mathcal{R} via the symmetry-breaking parameter κ and the role played by the aspect ratio L_x of the domain. Linear stability analysis shows that the base state is stable for all $\kappa \in [0, 1]$ at the selected parameters $\phi = 35^\circ$ and $Ra = 100$ indicating that all of the spatially localized structures analyzed here coexist with the stable base state. In particular, we show that for $\kappa > 0$ all localized structures acquire a nonzero drift speed, and explore the resulting dynamics.

B. Numerical method and simulation setup

We use the spectral solver Dedalus [80] to conduct direct numerical simulations (DNS) of the fluid equations, solving Eq. (4) subject to the boundary conditions specified in Eqs. (5) and (6). The system is discretized spatially using the Fourier spectral method in the x direction and the Chebyshev spectral method in the z direction. A 2nd-order 2-stage diagonally implicit Runge-Kutta (DIRK) + explicit Runge-Kutta (ERK) time-stepping scheme (RK222) [81, section 2.6] is used, which is a hybrid time-stepping method combining implicit and explicit Runge-Kutta methods. In addition to the $L_x = 10$ domain considered in [32], simulations are systematically performed in large periodic domains ranging from $L_x = 10$ to $L_x = 160$ with the corresponding grid point numbers n_x ranging from 256 up to 4096, with n_x proportional to L_x . In the z direction, we keep the resolution fixed at $n_z = 64$ grid points. These horizontally extended domains allow us to understand more easily the generic properties of n -pulse ($n = 1, 2, 3, 4, 5$) localized structures and the impact of finite domain size on their dynamics. We first choose different initial conditions to reproduce steady spatially localized structures with one to five pulses when $L_x = 10$ and $\kappa = 0$ [32] and then use these steady spatially localized structures as initial conditions for $\kappa \neq 0$ simulations. For larger domains $\tilde{L}_x > 10$, we concatenate the

spatially localized structures obtained with $L_x = 10$ and $\kappa = 0$ with the trivial state $(\mathbf{u}, T, p) = (\mathbf{0}, 0, 0)$ elsewhere, thereby generating an initial condition for simulations on the wider domain \tilde{L}_x , still with $\kappa = 0$. We let the simulation with such a concatenated initial condition evolve to a steady state, and then use the result as the initial condition for $\kappa \neq 0$ simulations with the corresponding domain size \tilde{L}_x .

III. CHARACTERIZATION OF n -PULSE TRAVELING STRUCTURES

In this section, we focus on the dynamics of traveling localized structures. Extensive DNS were conducted for different combinations of κ and L_x , generally resulting in n -pulse, traveling, spatially localized structures for $\kappa > 0$ owing to the breaking of the reflection symmetry \mathcal{R} , cf. [76–79]. Figures 2 and 3 show snapshots of the 2D profiles of n -pulse traveling convectons with $n = 1, 2, 3, 4, 5$ at two different values of κ in a domain of size $L_x = 40$. In each case the structures are shown at late times when they have reached a steady state in the comoving frame, with $\kappa = 0.01$ in Fig. 2 and $\kappa = 0.5$ in Fig. 3. When symmetry is only weakly broken ($\kappa = 0.01$), pulses in multi-pulse traveling spatially localized structures form bound states with small separation, as shown in Fig. 2, hereafter referred to as bound traveling localized structures. Similar bound states of individual pulses, also known as finite pulse trains, are widely observed in many problems featuring spatially localized structures, including reaction-diffusion systems with two [82] and three species [83, 84], and flowing thin films [85], to name only a few.

At strong symmetry-breaking (i.e. $\kappa \gtrsim 0.1$), pulses will repel each other, leading to the equispaced state shown in Fig. 3 at $\kappa = 0.5$. The distance between neighboring pulses in this state is equal to the domain size divided by the number of pulses, indicating that they reach the largest possible separation in the given finite domain. In some of the extreme cases where symmetry-breaking is sufficiently strong (κ close to unity) or the domain is particularly small, the spatially localized structures are unstable and decay to the base state. In this Section we select the domain size and κ to exclude this trivial case; the mode of instability of these states will be probed further in Sec. V. Considering the large number of parameter combinations (≈ 150) analyzed in this Section, we only consider relatively short DNS with simulation times between $t = 500$ and $t = 2000$ diffusive time units, corresponding to approximately 526 to 1152 CPU hours for each parameter combination. Long-time DNS results at selected parameters are presented in Sec. V.

A. Dependence of drift velocity on κ

Here, we investigate the dependence of the drift velocity c of spatially localized states on κ in the range of $\kappa \in [0, 1]$ and focus specifically on the range $\kappa \in [0, 0.1]$, where the symmetry is only weakly broken, for domain aspect ratios $L_x = 10$ and $L_x = 40$. Figure 4(a) shows the drift velocities c measured in different simulations of traveling spatially localized structures versus the symmetry-breaking parameter κ in a $L_x = 10$ domain. Panels (b) and (c) of Fig. 4 are both for $L_x = 40$, with (b) showing a zoom on the interval $\kappa \in [0, 0.1]$. We measure the velocity of the traveling spatially localized structures by tracking the x position associated with the maximum temperature deviation T at the midplane ($z = 0.5$) as a function of time. We then fit the discrete spatiotemporal data for constant velocity pulses with a linear function and use the fitted slope to define the drift velocity of each pulse. For structures with multiple pulses, we use the average velocity of all pulses composing the structure to represent the drift velocity of the entire spatially localized structure.

Based on the DNS results in Fig. 4(a) we conclude that when $L_x = 10$ the drift velocities c of n -pulse spatially localized structures are always positive and increase monotonically with the symmetry-breaking parameter κ . Here, the one- and two-pulse structures display a nonlinear law for the curve $c(\kappa)$, while localized structures with three to five pulses display a linear relation $c \propto \kappa$ (solid lines show fits). At a given value of κ , the relation between drift velocity and the number of pulses is also nontrivial. For example, Fig. 4(a) shows that for between one and four pulses, a larger number of pulses leads to a larger traveling speed c , while the five-pulse structure (where the pulses are deformed (not shown) due to finite-size effects in this small domain) travels more slowly than the three- and four-pulse structures.

Next, we investigate whether these relations between c and κ are robust in a larger domain. Figure 4(b) shows the drift velocity c over the same κ range $\kappa \in [0, 0.1]$ in the larger domain $L_x = 40$. The figure displays a quadratic relation between c and κ for all localized structures regardless of the number of pulses. Note that the drift velocity c is sign-indefinite for one, two, three and four pulses, meaning that these localized structures travel in the $-e_x$ (downslope) direction when κ is small, but reverse their travel direction as κ increases. In contrast to the non-monotonic relation between the drift velocity and the number of pulses in Fig. 4(a) for $L_x = 10$, spatially localized structures with more pulses travel at a larger (signed) velocity c when $L_x = 40$, given the same boundary conditions. Figure 4(c) shows the full κ range with $\kappa \in [0, 1]$, including the regime of stronger symmetry breaking, for $L_x = 40$. The drift velocities are seen to increase monotonically with κ for $\kappa \gtrsim 0.1$, and the $c(\kappa)$ curves deviate from the simple quadratic form

valid for small κ . In conclusion, the relation between the drift velocity of traveling spatially localized structures and the symmetry-breaking parameter κ is nontrivial and generically nonlinear. In addition, a comparison between the results from DNS in the computational domain $L_x = 10$ and $L_x = 40$ suggests that the domain size L_x has a strong impact on the dynamics of the traveling spatially localized structures studied here.

B. Dependence of drift velocity on domain size L_x

Next, we investigate the relation between drift velocity and domain size in more detail. We increased the aspect ratio from $L_x = 10$ to $L_x = 160$ by factors of 2 and varied the resolution from $n_x = 512$ to $n_x = 4096$ proportionally. Figure 5 shows a collection of space-time plots of a single-pulse structure traveling in domains of different sizes, from $L_x = 10$ to $L_x = 160$. Colors represent the temperature deviation at the midplane $z = 0.5$ so that the large-amplitude, inclined stripes in the space-time plots indicate travel. In the smallest domain, $L_x = 10$, the spatially localized structure travels in the e_x (upslope) direction and therefore has a positive drift velocity. When the domain size is increased to $L_x = 20$, the direction of travel reverses and the localized structure travels in the $-e_x$ (downslope) direction associated with a small, but negative drift velocity. As the domain size increases, the signed drift velocity decreases monotonically as shown in Fig. 5(f), appearing to saturate at an asymptotic value for large domain sizes.

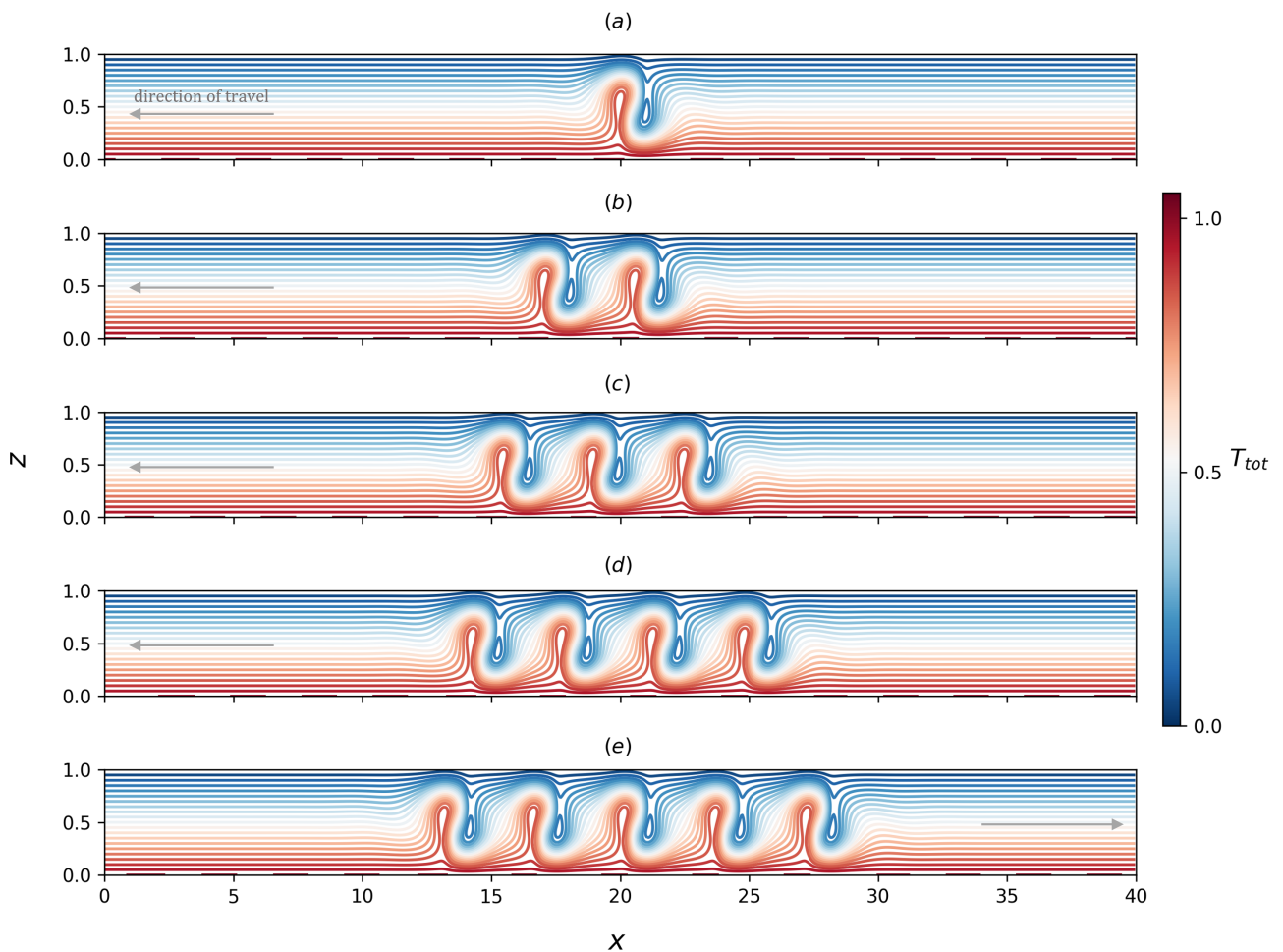


FIG. 2. Snapshots of the total temperature profile $T_{tot}(x, z)$ of n -pulse traveling spatially localized convective structures in a $L_x = 40$ domain, at $\phi = 35^\circ$, $Ra = 100$, and $\kappa = 0.01$. At this value of κ , traveling spatially localized structures form bound states. Panels (a)–(e) show spatially localized structures consisting of one to five pulses.

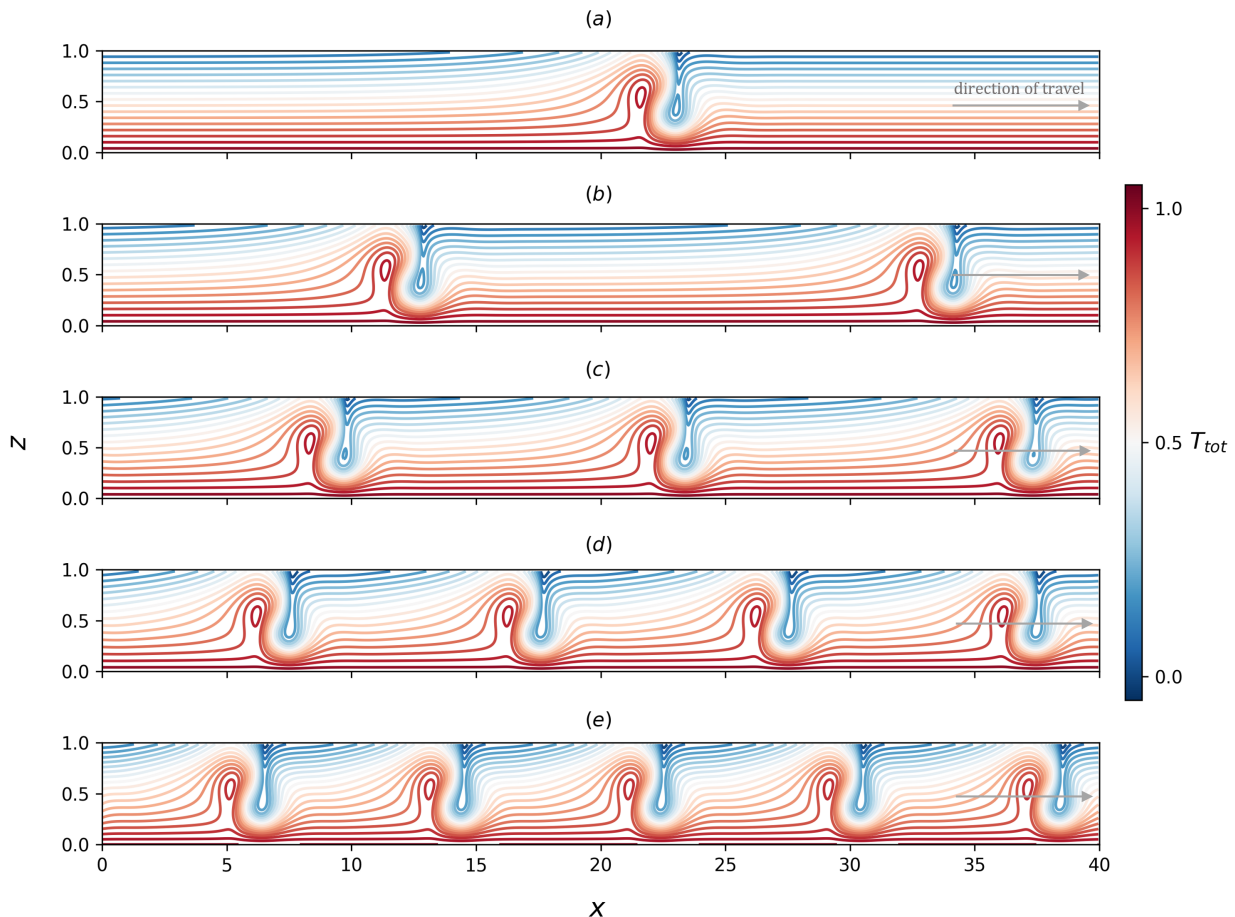


FIG. 3. Snapshots of the total temperature profile $T_{tot}(x, z)$ of n -pulse traveling spatially localized convective structures in a $L_x = 40$ domain, at $\phi = 35^\circ$, $Ra = 100$, and $\kappa = 0.5$. At this value of κ , traveling spatially localized structures converge to an equispaced configuration at late times. Panels (a)–(e) show states consisting of one to five pulses.

Different dynamics originating from domain size differences can be attributed to the interactions between traveling spatially localized structures and their periodic copies. The repulsive interaction between periodic copies resembles the interaction of adjacent pulses in multi-pulse traveling spatially localized structures in DNS. For example, the single pulse travels at $c \approx 0.4968$ for $\kappa = 0.1$ and $L_x = 10$ in Fig. 5(a), which is the same value of c (to three decimal places) as the equidistant four-pulse structures with $\kappa = 0.1$ and $L_x = 40$ in Fig. 4(b). Moreover, the trend in Fig. 5(f) that the signed drift velocity decreases with increasing domain size L_x is also consistent with the trend in Fig. 4(b) and Fig. 4(c) that the signed drift velocity decreases as the number of pulses is decreased for a given domain size, leading to wider spacing between pulses.

C. Unstable states at large κ

Our DNS results suggest that traveling spatially localized structures can be unstable for certain domain sizes L_x and symmetry-breaking parameters κ . This instability of traveling localized structures is typically associated with strong symmetry breaking (i.e., large κ) or small spacing of pulses due to a large number of pulses for a given domain size. A combination of both factors greatly increases the likelihood of instability. For example, DNS in a $L_x = 10$ domain with $\kappa \geq 0.2$ reveal that a five-pulse state is unstable, leading us to focus on the range $\kappa \in [0, 0.1]$ in Fig. 4(a),

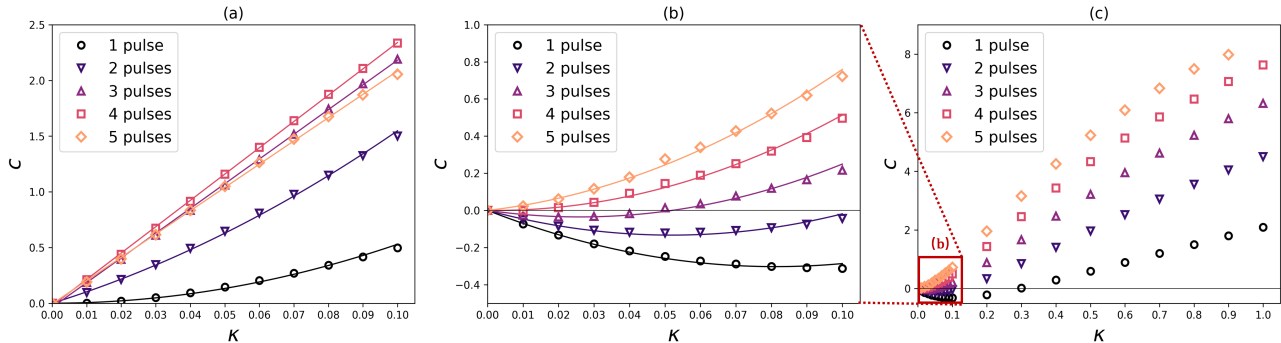


FIG. 4. Drift velocity c over the symmetry-breaking parameter κ for spatially localized structures consisting of one to five pulses within a domain of size $L_x = 10$ [panel (a)] and $L_x = 40$ [panels (b) and (c)]. Panel (b) gives a close-up view of panel (c) in the weak symmetry-breaking regime $\kappa \in [0, 0.1]$. For spatially localized structures with more than one pulse, the velocities of individual pulses are measured from DNS, and the average of these velocities is taken as the drift velocity c and plotted in markers in the figure. In panel (a), $c(\kappa)$ for single-pulse and two-pulse spatially localized structures are fitted with quadratic curves, while those for three- to five-pulse structures are fitted with linear curves. In panel (b), $c(\kappa)$ for single- to five-pulse structures is fitted with quadratic curves. Note that in panel (c) the velocity of the five-pulse spatially localized structure at $\kappa = 1$ is absent because the structure is unstable and spontaneously decays into a four-pulse spatially localized structure. Panels (b) and (c) further indicate that in the domain of size $L_x = 40$, the velocity c changes sign as κ is increased for one, two, three or four pulses ($c < 0$ at $\kappa = 0.01$ for four pulses), with downslope motion at small κ and upslope motion for larger κ .

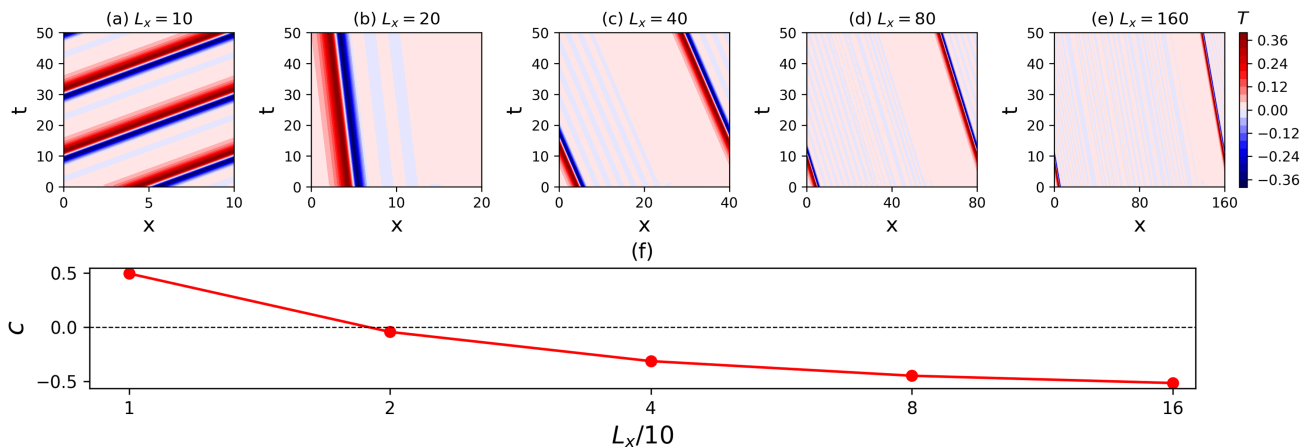


FIG. 5. Panels (a)-(e) show space-time plots of the temperature deviation $T(x, z = 0.5, t)$ at the midplane $z = 0.5$ of a single-pulse spatially localized structure traveling in domains of different aspect ratios L_x at $\kappa = 0.1$. Panel (f) shows the drift velocity c as a function of the domain aspect ratio L_x . The horizontal axis of panel (f) represents $0.1L_x$ and is plotted on a logarithmic scale of base 2, so that the points represent $L_x = 10, L_x = 20, L_x = 40, L_x = 80, L_x = 160$.

where such structures are stable. Increasing the domain size can suppress this instability. For example, the unstable five-pulse structure at $\kappa = 0.2$, $L_x = 10$ is stable at the same value of κ in a $L_x = 40$ domain; the drift speed of this state is plotted in Fig. 4(c). Nevertheless, a sufficiently strong symmetry breaking in the boundary conditions can generate instability even in a larger domain. For example, at $\kappa = 1$, instability does occur in the case of a five-pulse structure within a domain of aspect ratio $L_x = 40$. For this reason, no velocity measurement is shown in Fig. 4(c) for the five-pulse structure at $\kappa = 1$, as no such stable structure exists at this value of κ . Among the cases displaying instability, there are two scenarios for the subsequent evolution:

- Case 1. Partial annihilation: The n -pulse traveling spatially localized structure spontaneously decays, after a finite time, into a traveling localized structure consisting of fewer pulses. In this process, one or more pulses in the multi-pulse structure decay. In an $L_x = 10$ domain such partial annihilation was observed at (a) $\kappa = 0.45$ where a four-pulse structure decays into a three-pulse structure, (b) $\kappa = 0.5$ and $\kappa = 0.6$ where a four-pulse structure decays into a two-pulse structure, and (c) $\kappa = 0.7$ and $\kappa = 0.8$ where a four-pulse structure decays

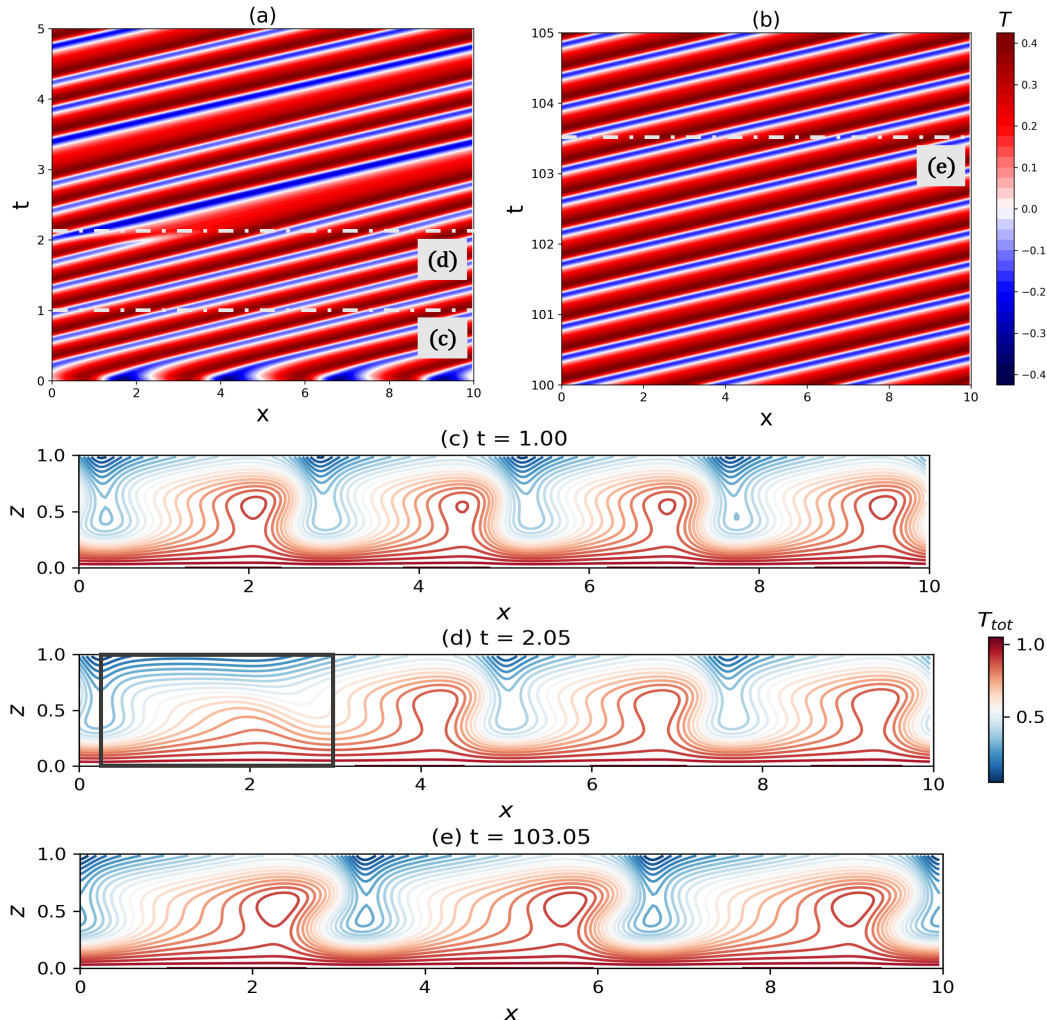


FIG. 6. Panels (a) and (b) show space-time plots of the temperature deviation $T(x, z = 0.5, t)$ at the midplane $z = 0.5$ of a traveling four-pulse localized structure in a $L_x = 10$ domain at $\kappa = 0.45$. Panels (c)-(e) show the total temperature profile $T_{tot}(x, z)$ at $t = 1$, $t = 2.05$, and $t = 103.04$, respectively, illustrating the initial stages of the transition from a four-pulse state to a three-pulse state via partial pulse annihilation indicated by the horizontal lines in panels (a) and (b). The black box in panel (d) highlights the collapsing pulse at $t = 2.05$.

into a single traveling pulse. Moreover, in a $L_x = 40$ domain with (d) $\kappa = 1$, a five-pulse structure decays into a four-pulse structure.

- Case 2. Spontaneous (complete) decay: The localized state cannot maintain its structure in the presence of sufficiently strong asymmetry in the boundary conditions and collapses to the base state. In an $L_x = 10$ domain such spontaneous decay was observed in the parameter interval (a) $\kappa \in [0.2, 1]$ within which five-pulse structures collapse to the base state, and (b) $\kappa \in [0.85, 1]$ within which four-pulse structures collapse to the base state.

Panels (a) and (b) of Fig. 6 show space-time plots and one-dimensional temperature profiles representing spatially localized structures at different stages of a transition from a four-pulse state to a three-pulse state described in Case 1 with $L_x = 10$ and $\kappa = 0.45$. A symmetric four-pulse initial state at $t = 0$ in a $L_x = 10$ domain rapidly becomes asymmetric owing to the finite value of κ ($\kappa = 0.45$, Fig. 6(c)) after which one of the constituent pulses suddenly collapses as can be seen in the space-time plot in Fig. 6(a) at $t \approx 2.05$. This is also shown in the snapshot of the 2D temperature profile in Fig. 6(d), where the leftmost pulse is seen to be decaying. As a result, one of the adjacent pulses expands into the void left by the decaying pulse. However, the resulting asymmetric state, with two narrow pulses and one wider pulse, is transient and gradually reorganizes itself into the regular three-pulse structure with

three identical pulses over time, while it continues to travel, with the pulses deforming and spreading out in the domain. Figure 6(e) explicitly shows that at a later time, all three pulses have become identical in shape and reached an equispaced configuration, identical to the final state observed at $\kappa = 0.45$ when initialized with a three-pulse state (from $\kappa = 0$). Similar partial annihilation of the traveling structure is also observed in a simulation initialized with a four-pulse state in an $L_x = 10$ domain at $\kappa = 0.5$, where two out of four pulses decay while traveling and the four-pulse structure evolves into a two-pulse final state. It is interesting to note that the drift velocity c of the ephemeral four-pulse structure prior to the collapse of the fourth pulse ($t \approx 1$) is very close to that of the three-pulse state at late time ($t \approx 100$). The spontaneous decay in Case 2 (not shown) likely indicates the presence of a fold where an n -pulse state ceases to exist, resulting in the collapse of the solution to the trivial state. Such behavior is characteristic of a subcritical state, an observation consistent with the results of [32].

IV. SPATIAL EIGENVALUES AND SPATIALLY LOCALIZED STRUCTURES

In the previous sections, we encountered the phenomenon of repulsion between neighboring pulses at strong symmetry breaking, which was shown in some cases to lead to equispaced, domain-filling structures. To elucidate the underlying mechanism of such a repulsive interaction, we analyze here the tail profiles of traveling spatially localized structures using spatial eigenvalues.

A. Spatial eigenvalues

Here, we linearize the equation of motion about the base state $(T_{bs}, \mathbf{u}_{bs}, p_{bs})$, and employ the notion of spatial dynamics [86, 87] to characterize the tail profiles of spatially localized structures in terms of spatial eigenvalues which have been extensively used to characterize spatially localized structures [40, 86–95], including in the Lugiato–Lefever equation [90] and in the Swift-Hohenberg equation [79, 96].

For the 2D flow considered here, we can express velocity in terms of a stream function ψ , so that $u = \partial_z \psi$ and $w = -\partial_x \psi$. Assuming a traveling-wave type solution of the form $\psi(x - ct)$, $T(x - ct)$ with a constant drift velocity c , we can write the following scalar governing equations, linearized around the base state $(T_{bs}, \mathbf{u}_{bs})$, as

$$(\partial_x^2 + \partial_z^2)\psi = Ra(\partial_z T \sin \phi - \partial_x T \cos \phi), \quad (7a)$$

$$-c \partial_x T + Ra \sin \phi \left(\frac{1}{2} - z \right) \partial_x T + \partial_x \psi = (\partial_x^2 + \partial_z^2)T. \quad (7b)$$

Reorganizing equations (7a) and (7b) into a spatial dynamics form yields

$$\partial_x \begin{bmatrix} \psi \\ \partial_x \psi \\ T \\ \partial_x T \end{bmatrix} = \begin{bmatrix} 0 & 1 & 0 & 0 \\ -\partial_z^2 & 0 & Ra \sin \phi \partial_z & -Ra \cos \phi \\ 0 & 0 & 0 & 1 \\ 0 & 1 & -\partial_z^2 & -c + Ra \sin \phi \left(\frac{1}{2} - z \right) \end{bmatrix} \begin{bmatrix} \psi \\ \partial_x \psi \\ T \\ \partial_x T \end{bmatrix} \quad (8)$$

with x playing the role of a time-like variable. The boundary conditions at the top ($z = 1$) and the bottom ($z = 0$) surfaces are

$$\partial_x \psi(z = 0) = \partial_x \psi(z = 1) = 0, \quad (9a)$$

$$T(z = 0) = 0, \quad (9b)$$

$$(1 - \kappa)T(z = 1) + \kappa \partial_z T(z = 1) = 0. \quad (9c)$$

We assume that the solution of this linear boundary value system takes the form

$$\begin{bmatrix} \psi \\ T \end{bmatrix} = \begin{bmatrix} \hat{\psi}(z) \\ \hat{T}(z) \end{bmatrix} e^{\lambda x} + c.c., \quad (10)$$

where λ is a spatial eigenvalue that can be obtained by solving Eq. (8) together with (9), and c.c. denotes the complex conjugate. We discretize the ∂_z operators in (8) using the Chebyshev differentiation matrix [97], and then solve for the spatial eigenvalues. Note that the drift velocity c of the traveling localized structure is needed in Eq. (8), but solving for c analytically remains challenging. For this reason, we resort to DNS to measure the drift velocity c of a single pulse traveling in a domain of aspect ratio $L_x = 160$ with the corresponding κ as done in Sec. III and substitute this value into the spatial eigenvalue computation in Eq. (8).

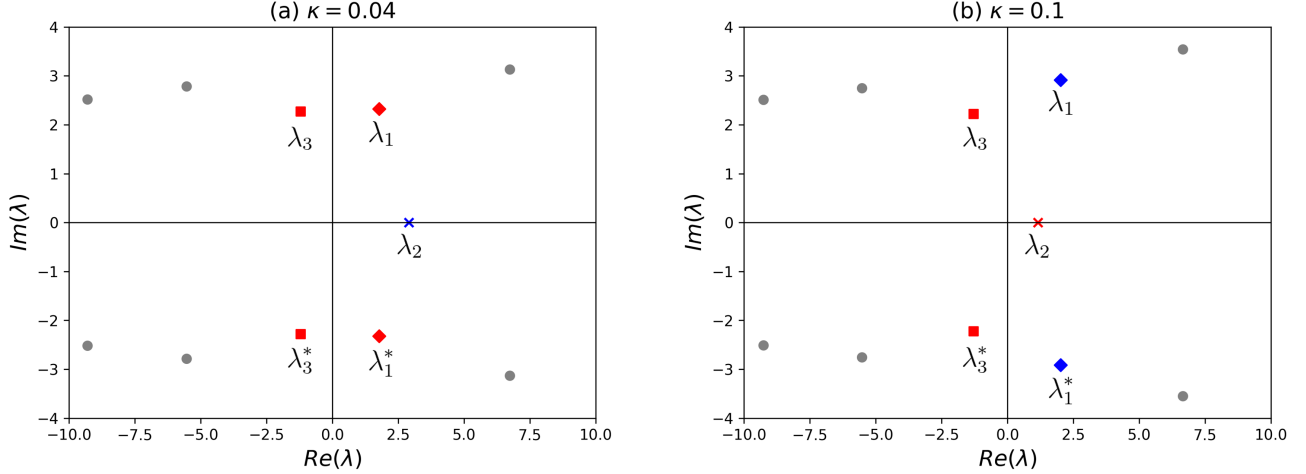


FIG. 7. The spatial eigenvalue spectrum shown in terms of the real and imaginary parts of the first 11 leading spatial eigenvalues near the origin for the traveling single-pulse localized structure in a domain of size $L_x = 160$ at (a) $\kappa = 0.04$ and (b) $\kappa = 0.1$. Red markers indicate the dominant spatial eigenvalues in each case. The alternation in color between red and blue for λ_1 (diamond markers) and λ_2 (cross markers) suggests a competition between real and complex spatial eigenvalues, which determines whether the downslope tail is monotonic or oscillatory. Meanwhile, λ_3 (square markers) remains dominant and determines the profile of the upslope tail.

In general, one expects the spatial profile of a pulse to approach the trivial state along the eigenvector corresponding to the spatial eigenvalue with the smallest magnitude of the real part, the contributions from the other eigenvalues having decayed earlier. In the following, we refer to such eigenvalues as dominant. The dominant spatial eigenvalues thus determine the profile of small-amplitude, exponential tails of the localized structures [91]. Real spatial eigenvalues indicate a monotonic tail, while complex eigenvalues indicate an oscillatory tail with the real part of the dominant spatial eigenvalue determining the spatial growth/decay rate of the exponential tail, while its imaginary part determines the wave number of the oscillatory tail. In the following, a tail is called ‘upslope’ if its amplitude decreases with e_x , behavior associated with dominant spatial eigenvalues whose real part is negative. We denote a tail as ‘downslope’ if its amplitude decreases in the $-e_x$ direction (i.e., increases in the e_x direction), corresponding to dominant spatial eigenvalues with positive real part.

Figure 7 shows the spectrum of the spatial eigenvalues at $Ra = 100$, $\phi = 35^\circ$ with the symmetry-breaking parameter (a) $\kappa = 0.04$ and (b) $\kappa = 0.1$. In Fig. 7(a), the dominant spatial eigenvalues consist of two pairs of complex conjugate eigenvalues λ_1, λ_1^* (with positive real part) and λ_3, λ_3^* (with negative real part). In Fig. 7(b) with stronger symmetry breaking, the dominant spatial eigenvalues consist of one real eigenvalue $\lambda_2 > 0$ and a pair of complex conjugate eigenvalues λ_3 and λ_3^* with negative real part. Thus the upslope tail is always oscillatory while the downslope tail may be monotonic or oscillatory, depending on whether $\lambda_2 < \text{Re}(\lambda_1)$ or vice versa.

In order to validate the predictions of the tail structure based on the spatial eigenvalue computations discussed above, we performed DNS of single-pulse localized structures traveling in a $L_x = 40$ domain, at (a) $\kappa = 0.04$ and (b) $\kappa = 0.1$. Their one-dimensional temperature deviation profiles in the midplane $T(x, z = 0.5)$ are shown in panels (a) and (b) of Fig. 8, respectively. At $\kappa = 0.04$, both the downslope and upslope tails are oscillatory, corresponding to complex dominant spatial eigenvalues λ_1, λ_1^* and λ_3, λ_3^* in Fig. 7(a). As expected, at $\kappa = 0.1$, the downslope profile is monotonic, corresponding to the real dominant spatial eigenvalue $\lambda_2 > 0$, while the upslope profile remains oscillatory, in agreement with the complex spatial eigenvalues λ_3, λ_3^* shown in Fig. 7(b). As the localized structures are traveling downslope ($-e_x$ direction) in Fig. 8, here the downslope tail can also be referred to as the leading tail while the upslope tail is the trailing tail.

Figure 8 compares the temperature profiles obtained in DNS with the tail structure predicted from the spatial eigenvalues. In the case of oscillatory tails, we present the spatial eigenvalue prediction as a function of the form $T(x, z = 0.5) = \gamma e^{\text{Re}(\lambda_i)x} \cos(\text{Im}(\lambda_i)x + \theta)$, where λ_i ($i = 1, 3$) is the dominant complex spatial eigenvalue, and the parameters γ and θ are determined by fitting this function to the DNS results. In the case of monotonic tails, a function of the form $T(x, z = 0.5) = \alpha e^{\lambda_2 x}$ is used instead, where λ_2 is the dominant real spatial eigenvalue and α is determined by fitting. As shown in Fig. 8, the midplane temperature profiles predicted by the spatial eigenvalues agree well with profiles obtained from the DNS results. We mention that hybrid configurations with both monotonic and oscillatory exponential tails, similar to those found here for $\kappa > \kappa_c$, have also been found in other systems, including

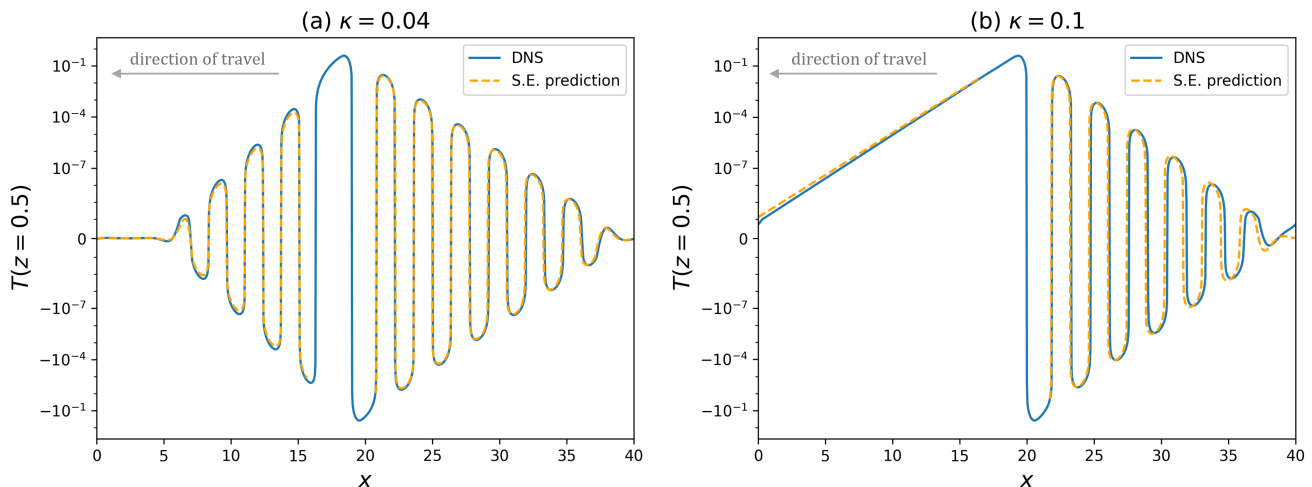


FIG. 8. Midplane temperature profile $T(x, z = 0.5)$ of traveling single-pulse spatially localized structure in a $L_x = 40$ domain as obtained from DNS at (a) $\kappa = 0.04$ and (b) $\kappa = 0.1$. The vertical axis is plotted on a symmetric logarithmic scale, with a cut-off at $T(x, z = 0.5) = \pm 10^{-10}$. The profiles in panels (a) and (b) correspond to the spatial eigenvalue predictions shown in Fig. 7. The orange dashed lines are the leading and trailing tails as predicted by the dominant spatial eigenvalues in Fig. 7.

the Kuramoto-Sivashinsky equation [98] describing a falling liquid film [99].

Furthermore, to quantitatively validate the spatial eigenvalue prediction, we can measure the spatial growth/decay rate of both oscillatory and monotonic tails and measure the wave number of the oscillatory tail by fitting the DNS result. For the oscillatory tail, we measure the average separation between local maxima representing wavelength ℓ leading to wave number $k = \frac{2\pi}{\ell}$. The growth/decay rates β of the oscillatory tails are obtained by fitting the discrete set of these local maxima to $T(x, z = 0.5) = \alpha e^{\beta_i x}$ ($i = 1, 3$). The downslope tails are characterized by $\beta_1 > 0$, while $\beta_3 < 0$ in the upslope tail, cf. Fig. 8. The monotonic tail is directly fitted with the function $T(x, z = 0.5) = \alpha e^{\beta_2 x}$ to obtain the spatial growth rate $\beta_2 > 0$ of the downslope tail.

Tables I and II compare quantitatively the spatial eigenvalue predictions against the spatial growth rate and wave number obtained from DNS of a single-pulse structure at $\kappa = 0.2$ in domains of various sizes by the fitting procedure described above. Here, we can see that the spatial eigenvalue prediction approaches the DNS results, with very good agreement for larger domain sizes, where the fitted DNS results become independent of the domain size. In particular, β_2 and β_3 in Tables I and II are almost independent of L_x when the domain size $L_x \geq 40$, for which the tail profiles have decayed to machine precision (double precision here). For example, we find $e^{\beta_3 L_x} = 1.25 \times 10^{-47}$ and $e^{-\beta_2 L_x} = 1.29 \times 10^{-22}$ when $\beta_3 = -1.35$, $\beta_2 = 0.63$, and $L_x = 80$.

The dependence of the spatial eigenvalue predictions (λ_2 and λ_3) on the domain size arises entirely from changes in the drift speed c as determined from DNS (Table I). As shown in Sec. III, the domain size has a significant impact on the drift speed of traveling localized structures: as L_x increases, the drift speeds measured in DNS reflect better and better its behavior in an infinite domain, leading to a more accurate spatial eigenvalue prediction. There are in fact two distinct contributions that set the speed c in an inclined domain, the interaction between the tails of the pulse and its periodic images upslope and downslope, and the asymmetry in the buoyancy profile at the pulse location when κ is nonzero. Figure 9 illustrates this asymmetry in the mean temperature profile, $\bar{T}(z)$, and the horizontal velocity in the comoving frame, $\bar{u}(z) - c$. In sufficiently large domains the former almost vanishes (i.e., $\bar{T}(z)$ is almost antisymmetric), while the latter does not. The latter drives distinct corrections to the base flow (the mean flow correction $\bar{u} - c$ along the bottom boundary differs from that along the top boundary). Because of the asymmetry between the upslope and downslope tails when $\kappa > 0$, changes in L_x (and hence in c) affect β_2 and β_3 differently, although both depend on L_x only weakly. Moreover, c appears to have a stronger dependence on the domain size L_x than either β_2 or β_3 (Table I). Figure 10 shows why this is so. The figure shows that the tail profiles of $T(x, z = 0.5)$ (and hence β_2 and β_3) have converged by $L_x = 80$ but that both $u(x, z = 0.5)$ and $u(x, z = 0.16)$ (and hence c) continue to exhibit domain size dependence at this value of L_x . However, both c and the associated change in c remain small compared with the background mean flow $\mathbf{u}_{bs} = Ra \sin \phi(\frac{1}{2} - z)\mathbf{e}_x$ with $Ra = 100$ as here, and so represent a small effect. The pointwise behavior shown in Fig. 10 thus differs substantially from that exhibited by the mean profiles \bar{T} and \bar{u} in Fig. 9.

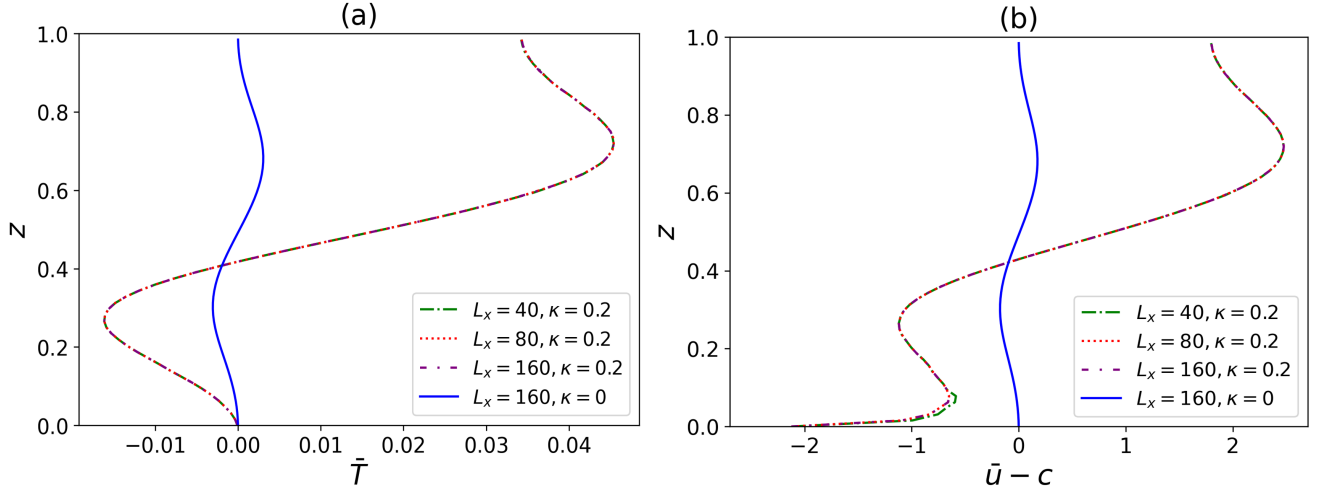


FIG. 9. Horizontally averaged profiles of (a) the temperature $\bar{T}(z)$ and (b) the horizontal velocity $\bar{u}(z) - c$ in the comoving frame. Each panel includes the mean profiles from DNS of a traveling single-pulse in domains of $L_x = 40, 80$ and 160 at $\kappa = 0.2$, with the corresponding spatial eigenvalues and drift velocity c provided in Table I. For comparison, the mean temperature and horizontal velocity profile of a stationary localized structure in an $L_x = 160$ domain with $\kappa = 0$ is also included (blue profiles). In both cases the averaged values are computed over the localized structure where $|T(x, z)| \geq 10^{-4}$.

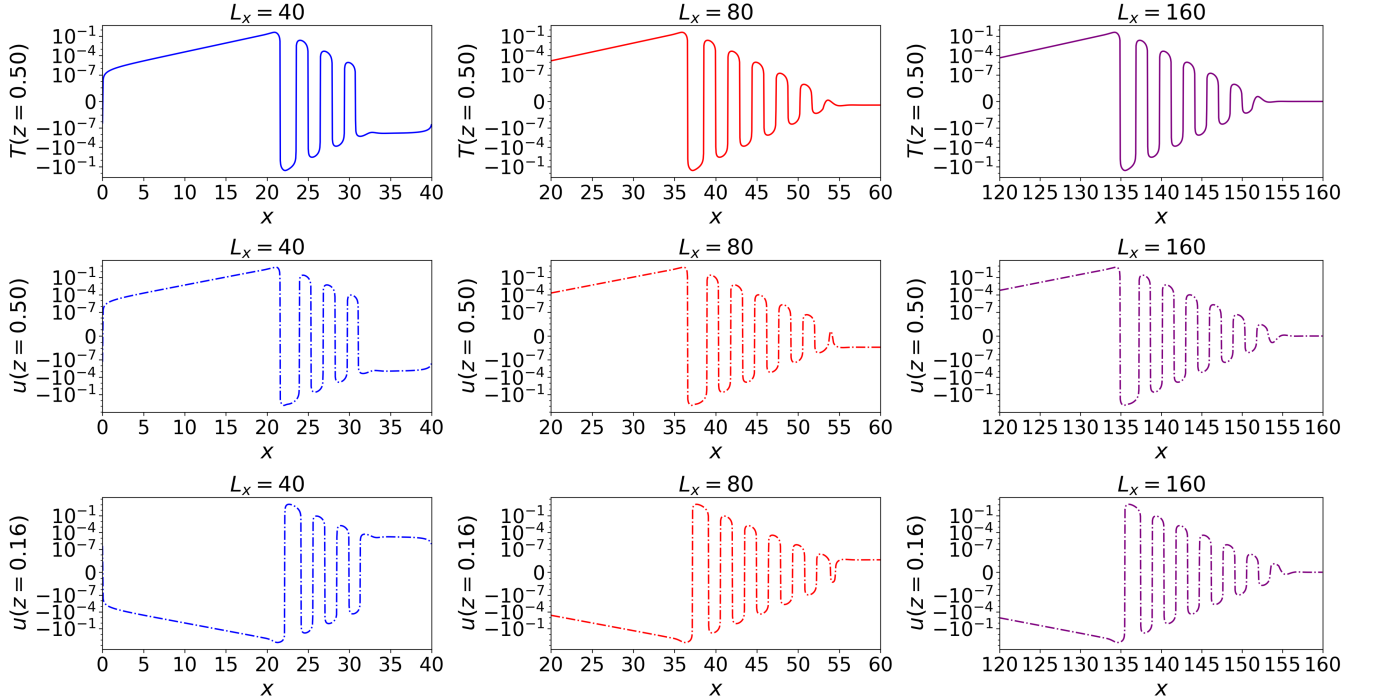


FIG. 10. Temperature deviation profiles $T(x, z = 0.5)$ (solid) and horizontal velocity deviation profiles $u(x, z = 0.5)$ (dash-dot) and $u(x, z = 0.16)$ (dash-dot) of traveling single-pulse states at $\kappa = 0.2$, in $L_x = 40, L_x = 80$, and $L_x = 160$ domains. All data are shown with a symmetric logarithmic y axis cutoff at $T(x, z) = \pm 10^{-10}$ and $u(x, z) = \pm 10^{-10}$. For the temperature field, profiles converge in domains with size $L_x \geq 80$. However, the velocity profiles exhibit noticeable differences between $L_x = 80$ and $L_x = 160$ at both the midplane and $z = 0.16$, indicating a different convergence rate compared with the temperature field.

Domain Size	$L_x = 20$	$L_x = 40$	$L_x = 80$	$L_x = 160$
DNS fitted spatial growth rate β_2	0.63499049	0.63502656	0.63496979	0.63498433
Spatial eigenvalue prediction of λ_2	0.5805	0.6058	0.6192	0.6260
Drift velocity c	0.3398	-0.2126	-0.4888	-0.6270

TABLE I. Spatial growth rate β_2 of the monotonic downslope tail fitted from DNS of the single-pulse localized structure at $\kappa = 0.2$ compared with the spatial eigenvalue prediction λ_2 using Eq. (8), together with drift velocities c obtained from DNS that are used for the spatial eigenvalue prediction in each domain.

Domain Size	$L_x = 20$	$L_x = 40$	$L_x = 80$	$L_x = 160$
DNS fitted spatial growth rate β_3	-1.29325158	-1.34512544	-1.34617153	-1.34414370
Spatial eigenvalue prediction of $\text{Re}[\lambda_3]$	-1.3254	-1.3345	-1.3402	-1.3434
DNS fitted wavenumber k	2.14466058	2.15905428	2.14943711	2.14943711
Spatial eigenvalue prediction of $\text{Im}[\lambda_3]$	2.3244	2.2340	2.1909	2.1698

TABLE II. Spatial growth rate β_3 and wave number k of the upslope oscillatory tail fitted from DNS of the single-pulse localized structure at $\kappa = 0.2$ compared with the spatial eigenvalue prediction λ_3 from Eq. (8). Drift velocities c used for spatial eigenvalue prediction are the same as shown in Table I.

B. Transition in tail structure predicted by spatial eigenvalues

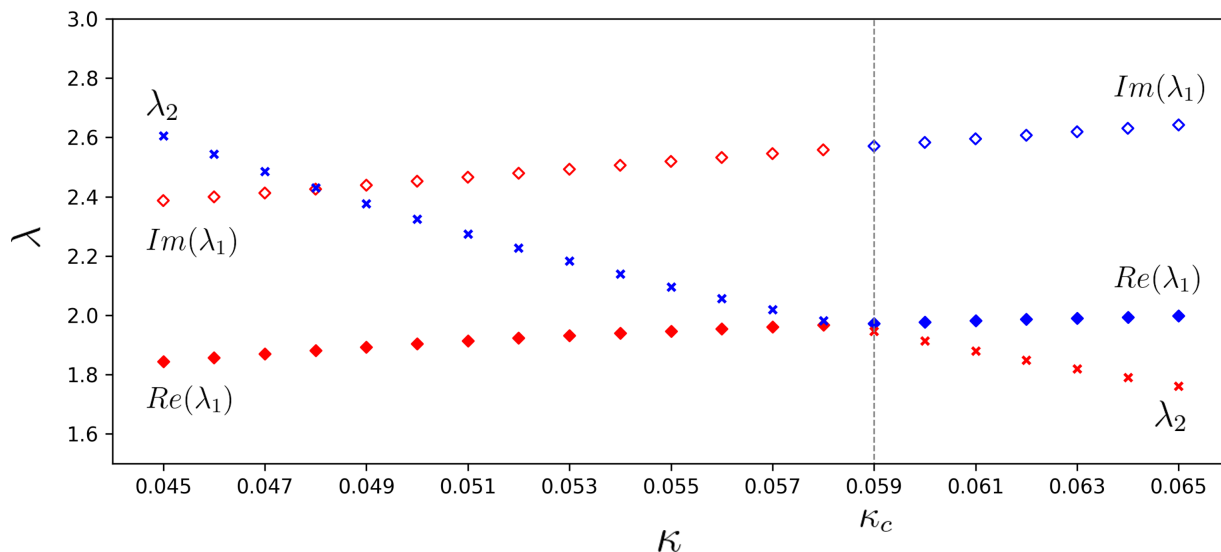


FIG. 11. Spatial eigenvalues λ_1 (diamond markers) and λ_2 (cross markers) associated with the downslope tail of a traveling single-pulse state as a function of κ . Red markers indicate the dominant spatial eigenvalues. When $\kappa < \kappa_c$, the tail is dominated by λ_1 and its complex conjugate λ_1^* , and is therefore oscillatory; when $\kappa > \kappa_c$, the tail is dominated by λ_2 , and is monotonic.

Figure 8, discussed earlier, shows that the (leading) downslope tail of the traveling spatially localized structures can be oscillatory or monotonic depending on the value of κ . This property is determined by the competition between the complex eigenvalues λ_1, λ_1^* and the real eigenvalue λ_2 shown in Fig. 7. In order to understand when the transition in tail structure occurs, we computed the spatial eigenvalues associated with the leading downslope tail in the regime of weakly broken symmetry (small κ). Figure 11 shows that as κ increases, $\text{Re}(\lambda_1)$ increases while λ_2 decreases. At a critical value of $\kappa_c \approx 0.059$, there is a crossover where for $\kappa > \kappa_c$, λ_2 takes over the role of the dominant eigenvalue from λ_1 , i.e., λ_2 has a real part closer to the origin than λ_1 . This process and a similar picture can be found in the work of Knobloch and Yochelis [91] on a multivariable reaction-diffusion system, where a similar exchange point plays a key role.

The spatial eigenvalues shown in Fig. 11 suggest that for a value of κ below the critical value κ_c , the downslope tail of the traveling spatially localized structures is oscillatory. For κ above the critical value κ_c , the downslope tail becomes monotonic. To confirm this transition in terms of the tail structure, we simulate traveling single-pulse states

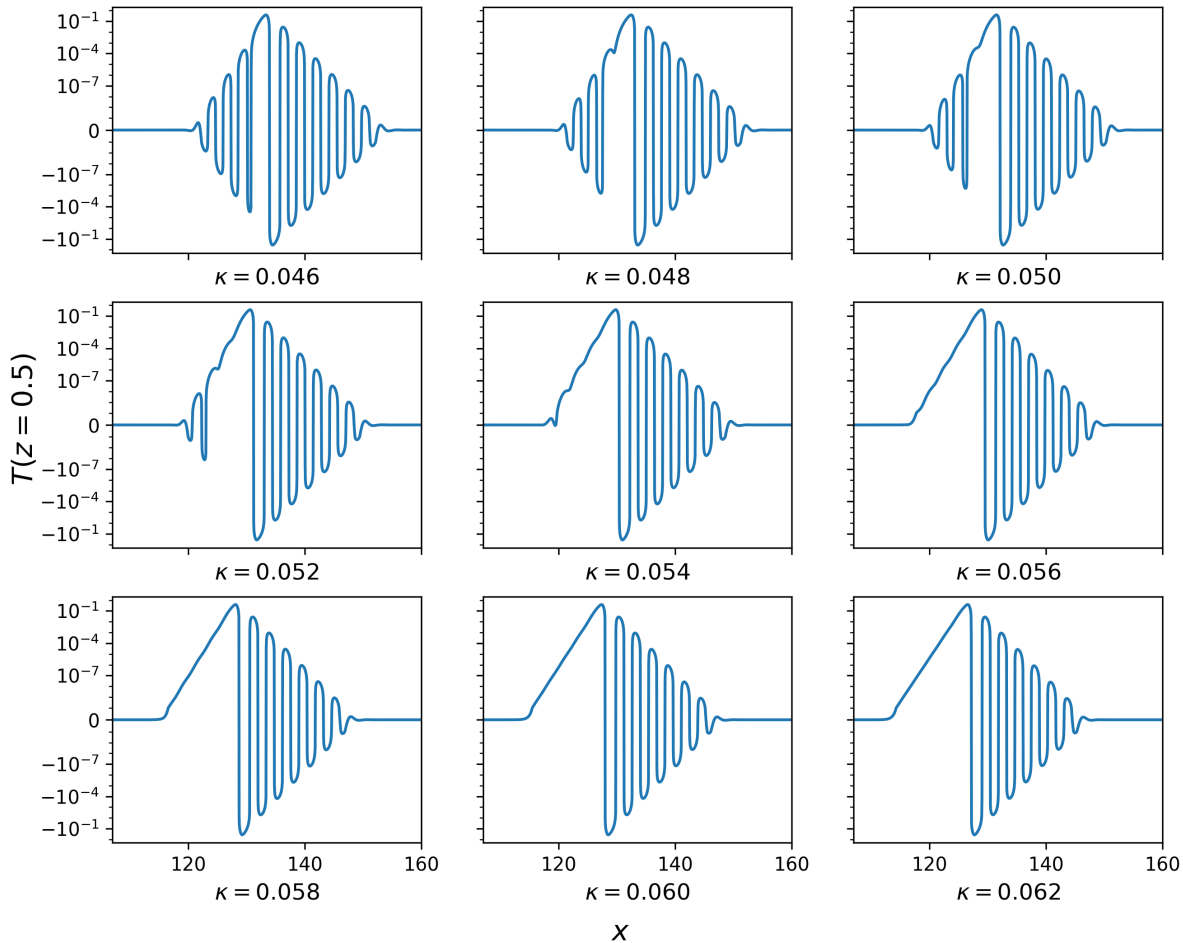


FIG. 12. Midplane temperature perturbation profiles $T(x, z = 0.5)$ of traveling single-pulse states at different values of κ in a wide domain with aspect ratio $L_x = 160$. All data is shown with a symmetric, logarithmic y axis cut off at $T(x, z = 0.5) = \pm 10^{-10}$. For all cases shown, the single-pulse structure travels downslope, i.e. in the $-\mathbf{e}_x$ direction. The leading (downslope) tails of the pulses are oscillatory when κ is well below $\kappa_c = 0.059$ and gradually morph into a monotonic, exponentially decaying profile as κ increases past κ_c (through a range where the two forms are superposed).

in a wide domain of aspect ratio $L_x = 160$ at different values of κ near the critical exchange point κ_c . Figure 12 shows how the downslope oscillatory tail of a traveling single-pulse state in a $L_x = 160$ domain gradually deforms into a monotonic tail as κ crosses the critical value κ_c . As shown in Fig. 12, at $\kappa = 0.046$, both tails of the localized structure are oscillatory. As κ increases, the downslope tail gradually becomes monotonic, while the upslope tail remains oscillatory, and the downslope tail becomes completely monotonic once κ is greater than the critical value $\kappa_c \approx 0.59$. The transition is gradual rather than abrupt, because when the real parts of λ_1 and λ_2 are comparable, a superposition of the two associated exponential tails emerges as a result. In summary, these observations confirm the existence of a critical value $\kappa = \kappa_c$ distinguishing different downslope tail profiles and the corresponding prediction based on spatial eigenvalues.

V. LONG-TIME TEMPORAL DYNAMICS OF INTERACTING LOCALIZED STRUCTURES

Section III shows that at late times, traveling states at small κ take the form of compact bound states (Fig. 2), while at large κ pulses repel each other leading to an equispaced state (Fig. 3). The long-range interaction between

spatially localized structures has been widely studied and is linked to the form of the exponential tails of these localized structures. Specifically, when the overlapping tails are both oscillatory (corresponding to complex spatial eigenvalues) then bound states exist generically, as established theoretically for numerous systems [100–105]. For instance, such multipulse bound states are found in the Swift-Hohenberg equation [106]. In contrast, in the case of monotonic tails (real spatial eigenvalues) localized structures typically repel one another, see e.g. [91, 107–110]. In the model considered here, the upslope tail of the localized structures remains oscillatory (complex spatial eigenvalue) as κ is increased, while the downslope tail undergoes a transition from oscillatory to monotonic form at the threshold $\kappa = \kappa_c \approx 0.059$. As a result, for $\kappa < \kappa_c$, the interaction between adjacent pulses is mediated by two oscillatory tails, which can potentially lock to one another, leading to bound states. By contrast, for $\kappa > \kappa_c$, the interaction between adjacent pulses is mediated by the overlap between a monotonic tail and an oscillatory tail, which typically leads to repulsion (but not in all cases, see also Sec. VI).

In this Section, we analyze further the long-time temporal dynamics of the repulsive interaction between traveling spatially localized structures by measuring the separation between pulses as a function of time at different values of κ . We extend selected DNS from Sec. III to investigate the long-time temporal dynamics of both bound and repelling traveling spatially localized structures, studying the time evolution of the inter-pulse separation in the vicinity of the threshold $\kappa = \kappa_c$.

A. Bound states for $\kappa < \kappa_c$

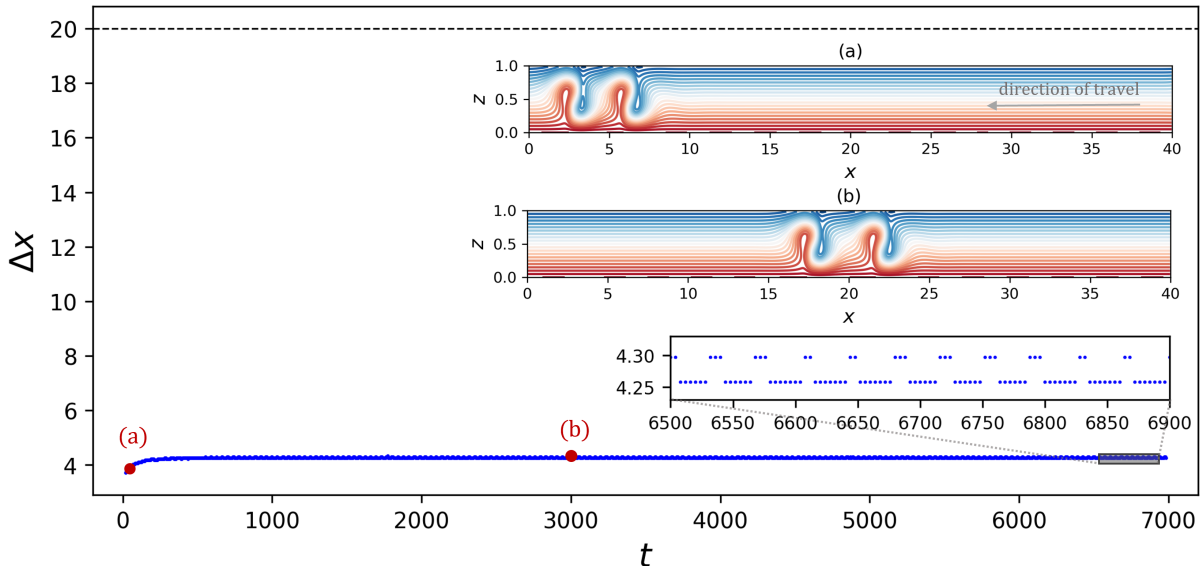


FIG. 13. Separation Δx between adjacent pulses versus time for a traveling two-pulse structure in a $L_x = 40$ domain, at $\kappa = 0.04 < \kappa_c$, together with their total temperature profiles $T_{tot}(x, z)$ at (a) $t = 21$ and (b) $t = 2960$. The separation between the two pulses increases with time and saturates at a distance of about $\Delta x = 4.25$. A zoom-in at the late time $t \in [6500, 6900]$ shows that the separation Δx fluctuates within one unit of grid resolution. This final separation is much smaller than the largest possible separation $\Delta x = 20$ (marked as dashed lines) for two-pulse localized structures in a $L_x = 40$ domain. Profile (b) also shows that the two-pulse structure is far from an equispaced traveling state, suggesting the existence of the traveling bound state.

In Fig. 2, we have already seen that for weak symmetry breaking (at $\kappa = 0.01$), traveling bound states of up to five pulses exist. Here, we first examine a traveling two-pulse structure in a $L_x = 40$ domain but with a slightly stronger (albeit still weak) symmetry breaking of $\kappa = 0.04$, which is near but still below the critical threshold κ_c . The separation between the pulses is measured over time as shown in Fig. 13. After a short initial transient, where the separation Δx between the two pulses increases only slightly, the configuration quickly converges to $\Delta x \approx 4.25$, with fluctuations within one unit of grid resolution, as shown in the zoom-in at late times in Fig. 13. This separation is significantly less than the maximum possible separation $\frac{1}{2}L_x = 20$, which indicates the presence of a true bound state, whose size is independent of L_x . The insets in Fig. 13 showing the total temperature profiles of the localized structures at an early time (a) and at a later time (b) further illustrate that the two pulses in the structure remain

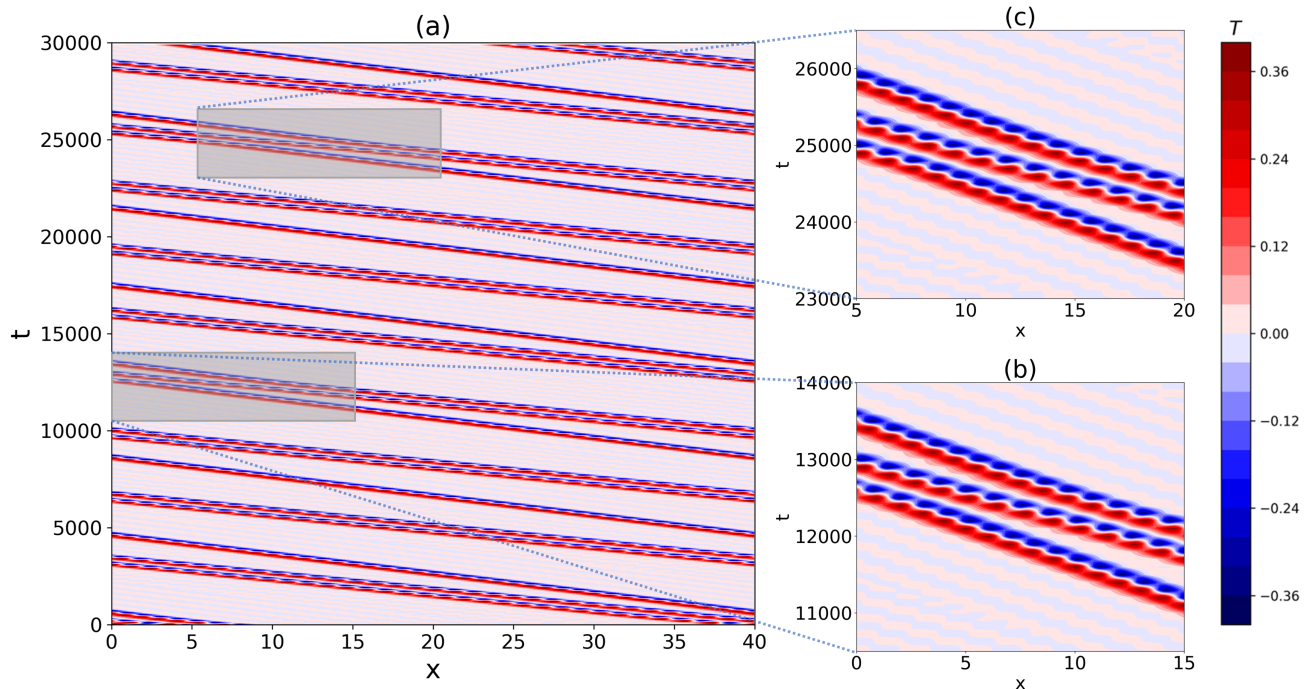


FIG. 14. Space-time plot, with time along the vertical axis and space along the horizontal axis, of a simulation initialized with a three-pulse spatially localized structure in a domain of aspect ratio $L_x = 40$ at $\kappa = 0.04 < \kappa_c$. Colors represent the midplane temperature deviation $T(x, z = 0.5, t)$. Panel (a) shows the space-time plot from $t = 0$ to $t = 30000$. Panels (b) and (c) zoom-in at the first and second collision between the deviated single pulse and the two-pulse bound state. The apparent modulation of the profile is a graphical artifact due to low output frequency; we reiterate that each pulse maintains its form while drifting, without any oscillations.

bound, with only a modest increase in separation, relative to the domain size, as the initial condition from $\kappa = 0$ adjusts to $\kappa = 0.04$.

While the four-pulse traveling bound state is also observed to be stable in $L_x = 40$ domain at $\kappa = 0.04$, (i.e., somewhat below the critical value κ_c), the three-pulse and five-pulse structures are found to be unstable at the same parameter values as a result of the repulsive interaction. As shown in Fig. 14(a), the right-most, trailing pulse in a flow initialized with a three-pulse spatially localized structure in a domain of aspect ratio $L_x = 40$ at $\kappa = 0.04$ detaches from the other two pulses, drifting downslope more slowly than the remaining two-pulse bound state. As these structures continue to travel, the single pulse is eventually caught by the two-pulse bound state due to periodicity and a collision ensues. The first such collision occurs at $t \approx 12000$, a zoom-in of which is shown in Fig. 14(b). In this collision, the bound state breaks up and one of the constituent pulses binds with the single pulse, accompanied by the repulsion of another single pulse on the other side, and the process repeats. The ensuing evolution appears to be cyclic, with a similar event occurring around $t \approx 25000$ [see Fig. 14(c)], resembling the motion of Newton's cradle resulting from a perfectly elastic collision. Similar behavior was also observed in a simulation initialized with a five-pulse spatially localized structure in a domain of aspect ratio $L_x = 40$ at $\kappa = 0.04$. Figure 15 shows related behavior resulting from an initial, unstable five-pulse structure at $\kappa = 0.04$, where a similar Newton's cradle-like behavior ensues. In contrast with the three-pulse case, here the structures travel in the positive (upslope) direction, with the trailing pulse gradually separating. However, in this scenario, this pulse is the leftmost pulse in the initial five-pulse structure. Due to periodicity, the detached single pulse is eventually caught by the four-pulse bound state at $t \approx 9500$ and the process repeats.

It is interesting to note that this type of instability of n -pulse states was only observed for $n = 3$ and $n = 5$, while two-pulse and four-pulse bound states were found to be stable over the long numerical integration time. This suggests that at this value of κ , the stability of n -pulse bound states depends on the parity of the integer n , with even n leading to stable bound states and odd n leading to instability via the detachment of the leading pulse. Further analysis will

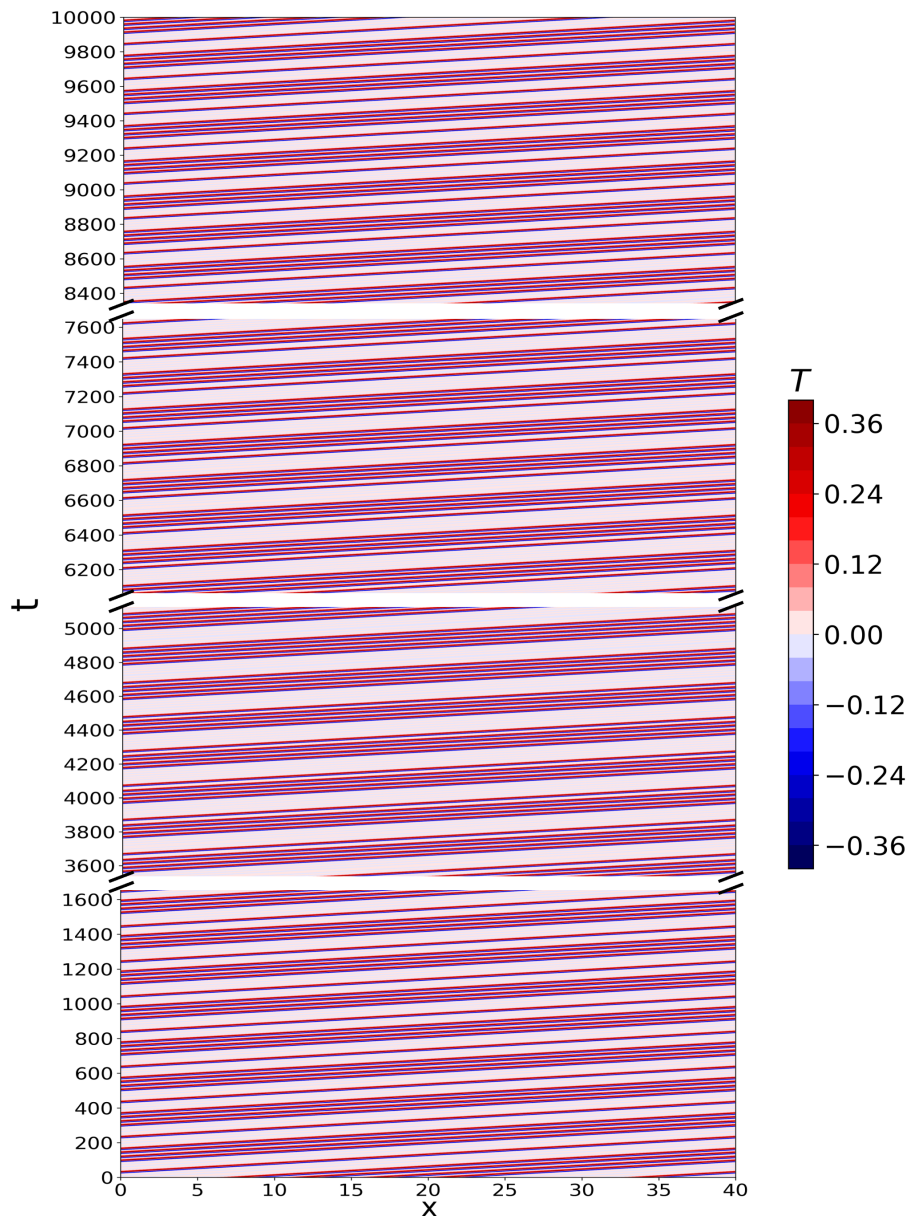


FIG. 15. Space-time plot of a traveling five-pulse structure in a domain of aspect ratio $L_x = 40$ at $\kappa = 0.04 < \kappa_c$. Colors represent the midplane temperature deviation $T(x, z = 0.5, t)$, shown with time along the vertical axis and space along the horizontal axis.

be needed to verify this hypothesis at larger values of n and to provide a theoretical explanation. This is left for a future study.

B. Repulsive interaction for $\kappa > \kappa_c$

In Fig. 3, we demonstrated that pulses with a monotonic tail repel each other leading to equispaced states in finite domains (here $L_x = 40$) for strong symmetry breaking (here $\kappa = 0.5$) and the coexistence of trains of between two and five pulses at identical parameter values. Similar equispaced traveling states were also observed in most cases where $\kappa > 0.5$, except when the traveling multi-pulse structures proved unstable, as in the case of the five-pulse structure at $\kappa = 1$.

However, just as the drift speed depends on κ and L_x as discussed in Sec. III, the interactions between pulses

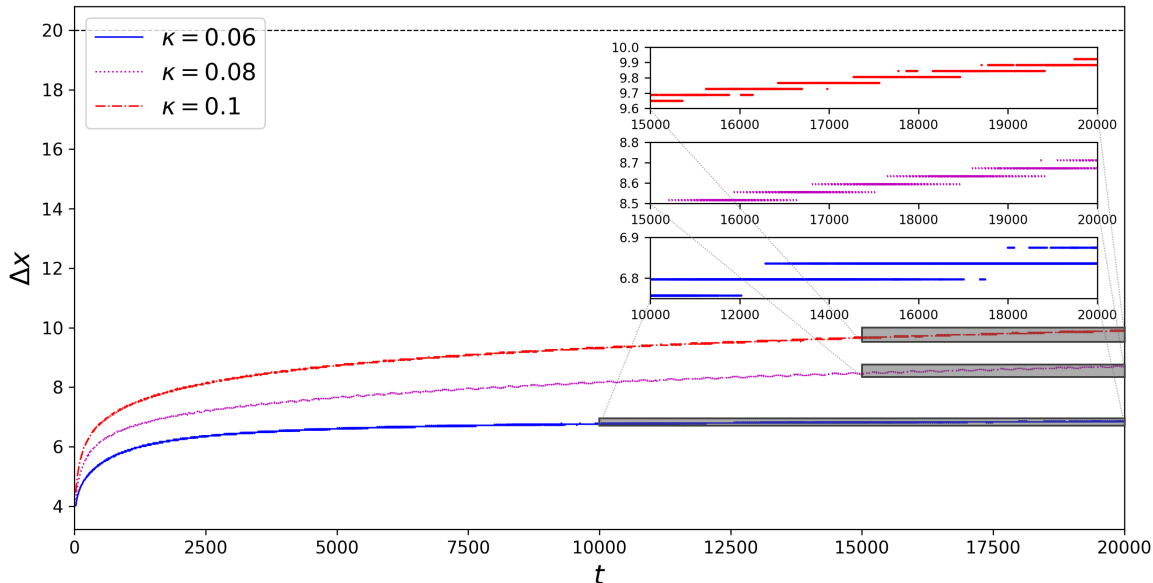


FIG. 16. Separation Δx between pulses versus time for a traveling two-pulse structure in a $L_x = 40$ domain, at $\kappa = 0.06$, $\kappa = 0.08$ and $\kappa = 0.1$, with zoom-ins on $\Delta x(t)$ in the time range $t \in [10000, 20000]$ for $\kappa = 0.06$ and $t \in [15000, 20000]$ for $\kappa = 0.08$ and $\kappa = 0.1$. Note that these curves are discrete because the increment in separation is now equal to the grid resolution 0.039.

can become exceedingly weak, particularly at small κ or in larger domains, requiring very long simulations in order to determine unambiguously whether the system converges to a bound state with a small distance between pulses, which is intrinsically determined and independent of the domain size, or an equispaced state where all pulses are at the maximum distance from each other for the given domain size. In our simulation of traveling two-pulse localized structures in a $L_x = 40$ domain, we confirmed that for $\kappa > 0.2$ the pulses consistently repel each other to the maximum possible separation of $\Delta x = 20$ (not shown). For simulations with $\kappa \in [\kappa_c, 0.2]$, no bound states at finite separations less than the largest separation ($\Delta x = 20$ in this case) have been observed although it remains numerically challenging to determine unambiguously whether the system converges to an equispaced configuration or not due to the very long time scales involved. Figure 16 shows the inter-pulse separation in a traveling two-pulse state versus time at $\kappa = 0.06, 0.08, 0.1$, respectively, with insets showing zoom-ins into the time interval $t \in [10000, 20000]$ for $\kappa = 0.06$ and $t \in [15000, 20000]$ for $\kappa = 0.08$ and $\kappa = 0.1$. Specifically, the separation between pulses in a traveling two-pulse spatially localized structure at $\kappa = 0.06$ only increases by four units of grid resolution in 10000 diffusive time units. This is notably different from the behavior of the converged separation curve, with fluctuations of only one unit of grid resolution, shown in Fig. 13, indicating that the traveling two-pulse structure has yet to reach its final separation at this value of κ . The slow dynamics shown in Fig. 16 prevent us from fully determining whether the final state will be a bound state or an equispaced state using DNS, despite a simulation time of $t = 20,000$. In Section VI we develop a reduced-order model that can be used to predict the final state in such parameter regimes.

In addition to the $L_x = 40$ domain, we also examined traveling two-pulse localized structures in an $L_x = 80$ domain and numerically confirmed the formation of equispaced traveling states at $\kappa = 0.95$. The separation between the two pulses is shown in Fig. 17. As the spatially localized structure travels, the constituent pulses repel each other and eventually reach a final state where they are equally spaced at half the domain size. The temperature deviation profiles at an early time (a) and a later time (b) clearly illustrate this change in separation over time, which contrasts sharply with the bound state observed at smaller κ values shown in Fig. 13.

While repulsion also occurs in traveling multi-pulse structures with more than two pulses, the spreading process can involve more complex dynamics than that of the two-pulse localized structure. Figure 18 illustrates the spreading dynamics resulting from the repulsive interaction. Panels (a), (b) and (c) of Fig. 18 show snapshots of the full temperature field at different stages of the process. At very early times (panel (a)), the right-most pulse (which is also the leading pulse in this case since the structure travels to the right, i.e. upslope), is propelled to the right the fastest. Subsequently, the second pulse from the right detaches and moves to the right faster than the pulses further

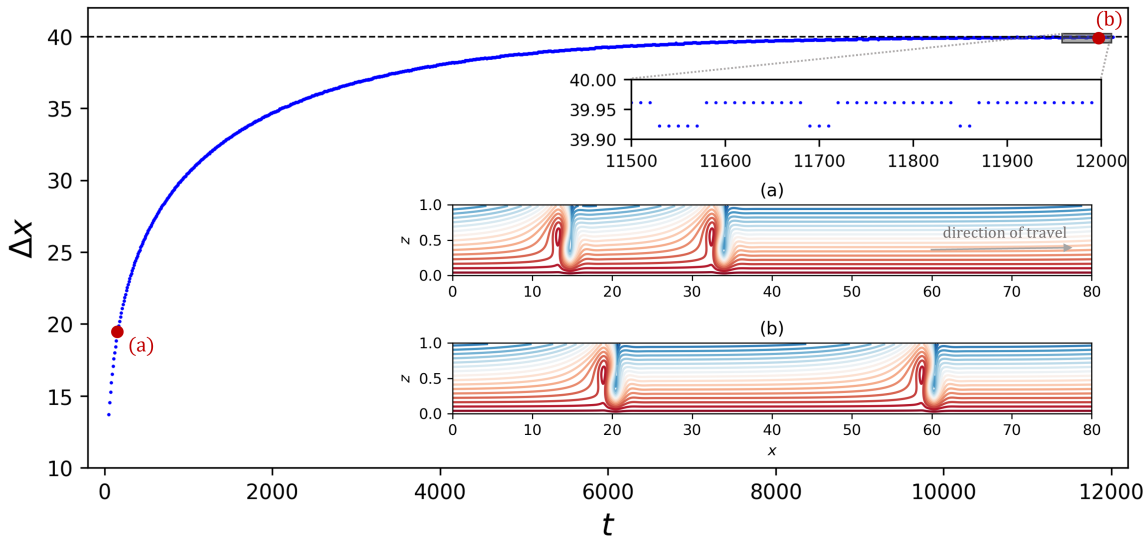


FIG. 17. Separation Δx between pulses versus time for a traveling two-pulse structure in a $L_x = 80$ domain, at $\kappa = 0.95$, and the corresponding total temperature profiles $T_{tot}(x, z)$ at (a) $t = 160$ and (b) $t = 11980$. The separation between the two pulses increases with time and converges to the largest possible separation, $\Delta x = 40$ for two pulses in a $L_x = 80$ domain. A zoom-in at the late time $t \in [11500, 12000]$ shows that the separation Δx fluctuates within one unit of grid resolution. As shown in profile (b), the traveling two-pulse structure is now equispaced in the domain.

to the left (panel (b)). At late times (panel (c)), the system reaches an equispaced configuration where all pulses have spread out evenly.

In Fig. 18(d), this evolution is quantified in terms of the separation between adjacent pulses over time. One observes that the separations systematically overshoot the final equidistant spacing, $\Delta x = 8$ here, with the rightmost pulse reaching the maximum separation from its adjacent pulse first, followed by the second from the right, etc. As t increases to late times (i.e., $t \gtrsim 100$), the separation curves saturate at $\Delta x = 8$ while undergoing damped, small-amplitude oscillations, a nontrivial feature given the absence of inertia from the system.

C. Collision between traveling bound states

The discovery of cyclic, Newton's cradle-like behavior of three-pulse and five-pulse traveling localized structures at $\kappa = 0.04 < \kappa_c$ motivates further investigation of collisions between traveling convectons in bound states. We utilized the drift velocity difference between traveling bound states with different numbers of pulses to set up chasing collision scenarios in DNS by concatenating two periodic domains in the x direction initialized with different n -pulse bound states.

Figure 19 shows collisions between a single pulse and bound states consisting of two (panel (a)) or three pulses (panel (b)) at $\kappa = 0.03$ in a combined domain of $L_x = 80$, formed by concatenating these two traveling localized structures within $L_x = 40$ domains. The collisions conserve the number of pulses, but are inelastic, producing simple combined bound states consisting of three and four pulses, respectively, without the creation or annihilation of pulses. This phenomenology differs from collisions reported previously in binary fluid convection [67], which are significantly impacted by fluid inertia, and in the bistable Swift-Hohenberg equation [43, 79], proposed as an order parameter description of spatially localized structures in binary fluid convection. In both cases, more complex dynamics ensue upon collision, including annihilation and creation of new pulses. Collisions of localized modulated traveling waves in binary fluid convection also lead to distinct behaviors [55, 56, 111], such as the gradual growth of the traveling wave envelope in the aftermath of the collision, similar to depinning dynamics [112], the annihilation of certain localized traveling waves, or the generation of new waves, none of which are observed here.

In addition to collisions of bound states, we find unstable structures in the combined domain when concatenating structures which are individually stable at sufficiently large κ . For example, at $\kappa = 0.5$, when concatenating a two-pulse traveling structure with a single-pulse structure in two $L_x = 40$ domains, both individually stable in this domain, the resulting state in a domain of size $L_x = 80$ spontaneously decays to the base state solution immediately

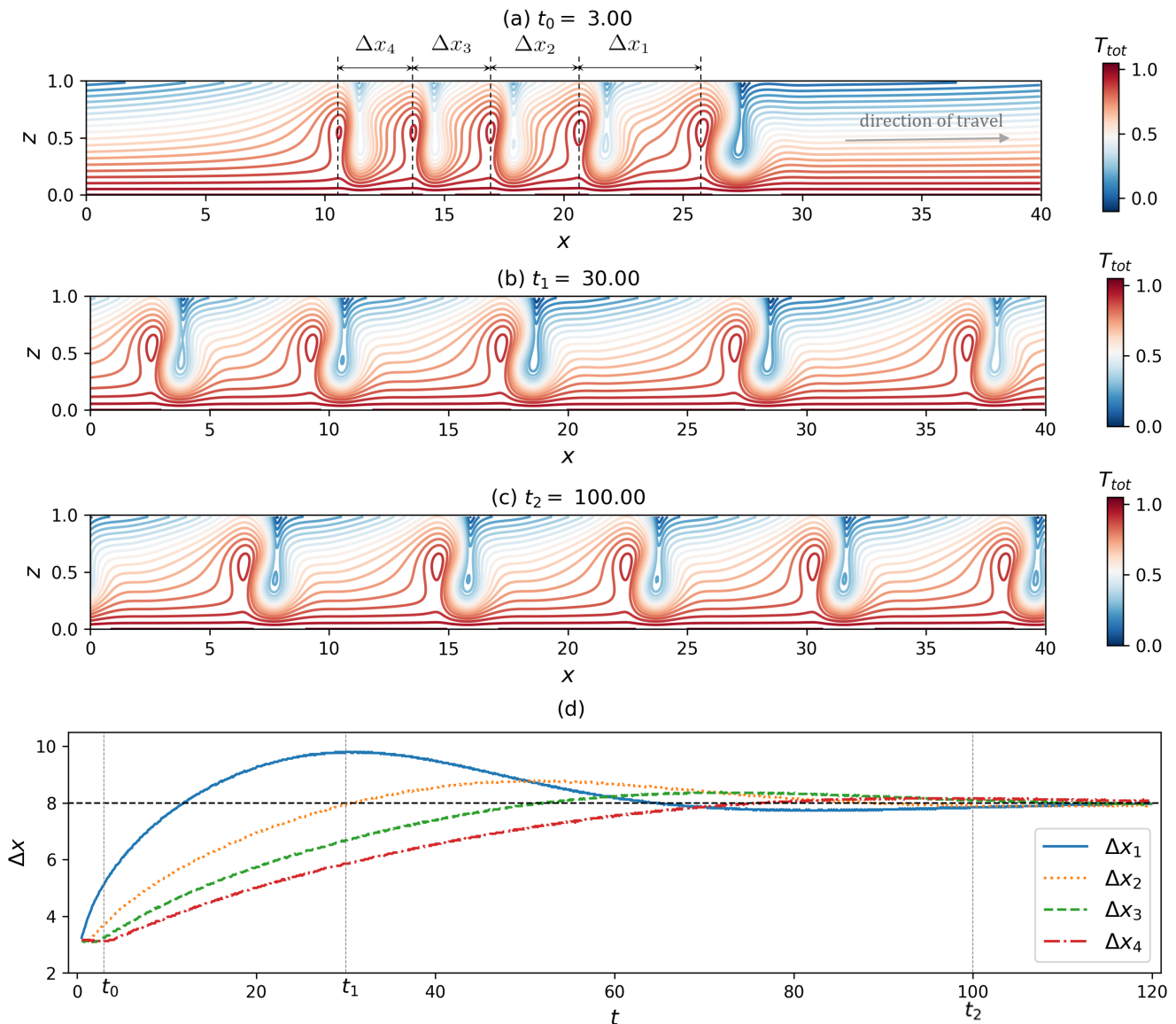


FIG. 18. Total temperature profiles $T_{tot}(x, z)$ of traveling spatially localized structures at time (a) $t_0 = 3$, (b) $t_1 = 30$, and (c) $t_2 = 100$ for a right-traveling five-pulse structure in a $L_x = 40$ domain with $\kappa = 0.9$. Separations between adjacent pulses are labeled Δx_i , $i \in \{1, 2, 3, 4\}$, as indicated in panel (a), and their time dependence is shown in panel (d). The largest possible separation between five pulses in the $L_x = 40$ domain, $\Delta x = 8$, is marked out in the black dashed line in panel (d). The leading pulse experiences the strongest repulsion over time, resulting in a stronger overshoot of the separation Δx_1 and faster convergence to the final equispaced state.

after initialization, in a manner identical to Case 2 reported in Sec. III C. This observation suggests a potential long-range interaction between localized structures (possibly mediated by incompressibility), though this requires further investigation. Another possible explanation is that the fold of the three-pulse state is located at a larger Rayleigh number than that of the one- and two-pulse states, but numerical continuation techniques will be needed to assess this hypothesis.

VI. REDUCED-ORDER MODELING

Long-range interactions between localized structures are mediated by their exponentially growing or decaying oscillatory tails. Such interactions via exponential tails are found in a wide range of problems and have been studied

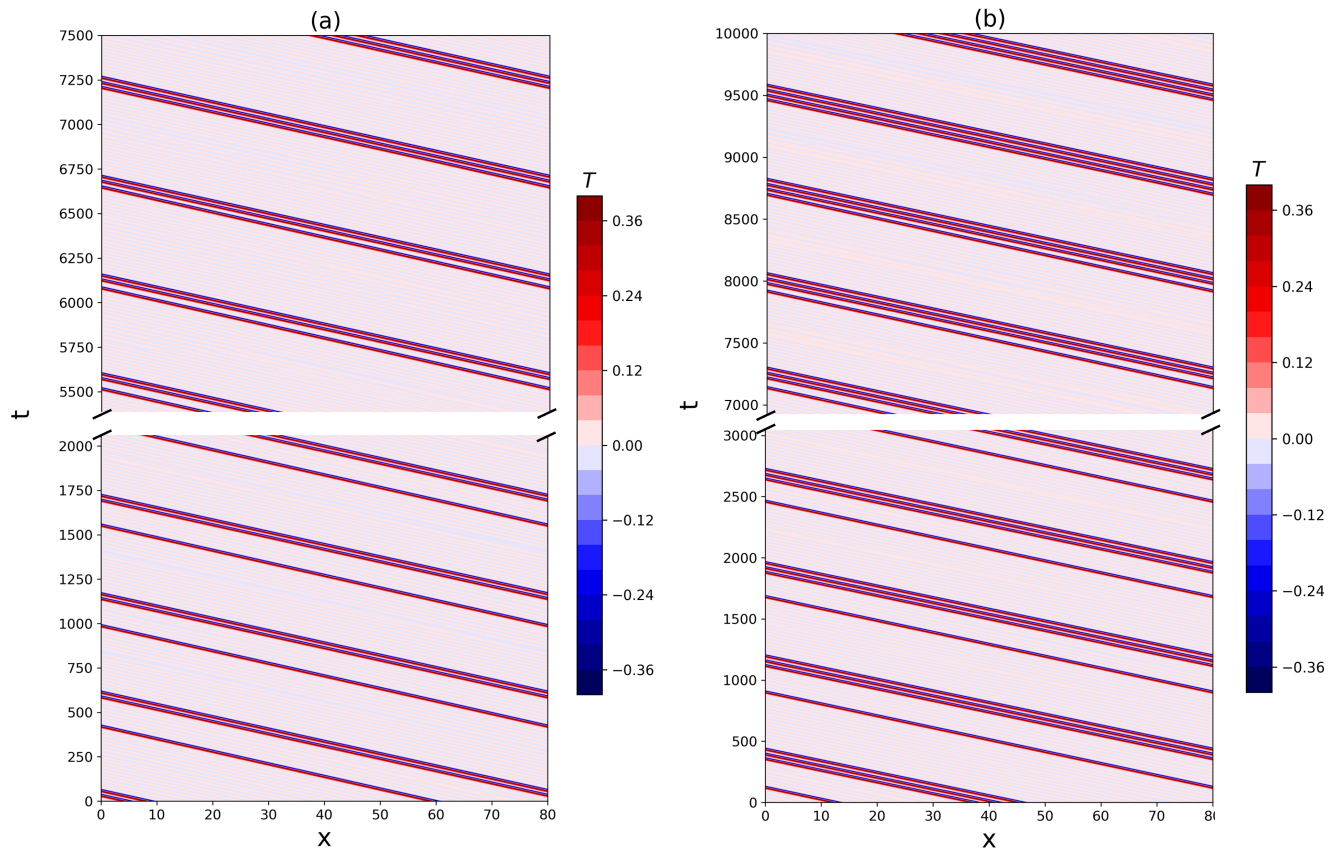


FIG. 19. Space-time plots of the midplane temperature deviation $T(x, z = 0.5, t)$ displaying collisions between a single pulse and bound states consisting of two (panel (a)) or three pulses (panel (b)) at $\kappa = 0.03$. The collisions are conservative, producing new bound states consisting of three and four pulses, respectively, without the creation or annihilation of additional pulses.

extensively, see e.g. [98, 107, 113–117]. Recently, in [79], a simple reduced-order model was introduced to quantitatively describe these interactions. This reduced-order model was shown to reproduce a wide range of collisions with quantitative accuracy for asymmetric spatially localized structures within the cubic-quintic Swift-Hohenberg equation (SH35) [79]. Here, we adapt this model to the problem at hand. This reduced-order model describes the intrinsic traveling behavior of each localized structure based on their phase speed as obtained from DNS in Sec. III. Superposed on this motion are effects of the pulse-pulse interaction described in a particle-like manner, modeled using the tail structures of the interacting pulses informed by the spatial eigenvalues λ_2 and λ_3 obtained in Sec. IV.

As in the DNS described above, we consider two localized structures whose proximate, large-amplitude maxima in $T(x, z = 0.5, t)$ [defined as those with $T(x, z = 0.5, t) > 0.3$] are located at positions x_1 and x_2 in $[0, L_x]$; the distance between the two proximate, finite-amplitude maxima is denoted by $\Delta x \equiv |x_2 - x_1|$. Each localized structure propagates at a given speed, denoted by c_1 and c_2 , in the absence of interactions, and interactions modify their propagation. The dominant spatial eigenvalue with positive real part is denoted by $\Lambda \equiv \Lambda_r + i\Lambda_i$, with $\Lambda = \lambda_1$ for $\kappa < \kappa_c$ and $\Lambda = \lambda_2$ for $\kappa > \kappa_c$ while $\lambda_3 = \lambda_{3r} + i\lambda_{3i}$ remains the dominant eigenvalue with negative real part for all κ . We take into account the finite domain size L_x and periodic boundary conditions to obtain the following reduced model equations, reminiscent of overdamped particle dynamics, but with a nontrivial interaction force:

$$\frac{dx_1}{dt} = c_1 + g_1 \cos(\Lambda_i \Delta x + \varphi) e^{-\Lambda_r \Delta x} + g_2 \cos(\lambda_{3i}(L_x - \Delta x) + \varphi) e^{\lambda_{3r}(L_x - \Delta x)}, \quad (11a)$$

$$\frac{dx_2}{dt} = c_2 + g_1 \cos(\Lambda_i(L_x - \Delta x) + \varphi) e^{-\Lambda_r(L_x - \Delta x)} + g_2 \cos(\lambda_{3i} \Delta x + \varphi) e^{\lambda_{3r} \Delta x}. \quad (11b)$$

Here g_1 and g_2 are unknown interaction amplitudes and φ is an unknown interaction phase. We stress that the g_1 in Eqs. (11a) and (11b) are identical since they both describe the interaction with a downslope tail, while g_2 is likewise identical between Eqs. (11a) and (11b). These three unknown parameters, g_1 , g_2 and φ , are determined by least-square

fitting of x_1, x_2 to DNS data, see [79]. In principle, there could be distinct phases φ_1, φ_2 when two oscillatory tails are present, but it is found empirically that one phase is sufficient to accurately reproduce DNS results. The model can be generalized to more than two interacting pulses, but we restrict attention to two interacting localized states only. We compare DNS and reduced model results in two cases: (1) a repulsive interaction where one tail is monotonic and the other oscillatory tail, and (2) a chasing collision between a single pulse and a two-pulse bound state where both tails are oscillatory.

A. Repulsion for $\kappa > \kappa_c$

As in the DNS results shown in Fig. 17, we consider an initial two-pulse state composed of two identical single-pulse structures at $\kappa = 0.95$ [where $\Lambda = \lambda_2 \in \mathbb{R}_+$, i.e., $\Lambda_i = 0$ in Eq. (11)] in a domain of size $L_x = 80$. In isolation, each pulse travels with the same velocity $c_1 = c_2$. In this case, the only equilibrium of Eq. (11) is $\Delta x = L_x/2$. Indeed, this is confirmed by integrating the ODEs using a fourth-order Runge-Kutta time-stepping scheme, starting from the same initial positions of the pulses as in the DNS. Figure 20(a) shows trajectories in the comoving frame of two interacting pulses at $\kappa = 0.95$ in a domain of size $L_x = 80$ from the reduced model in Eq. (11) with parameters estimated by fitting the trajectories to the corresponding DNS data. The right-most pulse is propelled to the right faster initially, as seen in all repulsive interactions in DNS, cf. Fig. 18. Figure 20(b) shows a comparison, for two interacting pulses at $\kappa = 0.95$ in $L_x = 80$, between the separations $\Delta x(t)$ obtained from DNS (cf. Fig. 17) and the model result. The two curves agree well and we conclude that the particle-like dynamics of Eq. (11) correctly describe the observed repulsion between localized pulses.

For a better understanding of the possible equilibrium values of Δx when $\Lambda = \Lambda_r \in \mathbb{R}_+$, we subtract Eq. (11a) from Eq. (11b), with $c_1 = c_2$, assuming $x_2 > x_1$ without loss of generality, to obtain

$$\frac{d\Delta x}{dt} = g_1 \cos \varphi \left[e^{-\Lambda_r(L_x - \Delta x)} - e^{-\Lambda_r \Delta x} \right] + g_2 \left[\cos(\lambda_{3i} \Delta x + \varphi) e^{\lambda_{3r} \Delta x} - \cos(\lambda_{3i}(L_x - \Delta x) + \varphi) e^{\lambda_{3r}(L_x - \Delta x)} \right] \equiv f(\Delta x). \quad (12)$$

Figure 21 shows the function $f(\Delta x)$ for three cases in a domain of size $L_x = 80$ (obtained using $g_1 = -g_2$, $\varphi = 0$, as in Fig. 20). At $\kappa = 0.95$ [panel (a)] and $\kappa = 0.1$ [panel (b)], the function $f(\Delta x)$ only has one root, $\Delta x = L_x/2 = 40$. The significantly smaller values of $f(\Delta x)$ at $\kappa = 0.1$ compared to $\kappa = 0.95$ indicate a drastic slowing-down of the repulsion. In contrast, at $\kappa = 0.08$ [panel (c)], there are oscillations leading to a large number of roots, corresponding to bound state separations, half of which are stable equilibria and the other half unstable. The critical difference between the three cases is the relative size of Λ compared with $|\lambda_{3r}|$ that controls which tail is more extended. For $\Lambda < |\lambda_{3r}|$ (monotonic tail longer than oscillatory tail), one finds numerically that the only root of $f(\Delta x)$ systematically occurs at $\Delta = L_x/2$, independently of L_x , and corresponds to a stable equilibrium, in agreement with Fig. 20(b). However, this does not remain true for $\Lambda \geq |\lambda_{3r}|$ (oscillatory tail longer than monotonic tail), which is the case for weakly supercritical $\kappa \gtrsim \kappa_c$ (see Fig. 7), and/or $|g_2| \gg |g_1|$, in which case there are systematically multiple equilibria of Eq. (11) corresponding to multiple possible bound state separations. We note for completeness that for $|g_2| \gg |g_1|$ (a case which we did not observe in DNS) the function $f(\Delta x)$ has several roots even when Λ is smaller than $|\lambda_{3r}|$. These findings complement the DNS results in Fig. 16, where convergence could not be reached due to limited simulation time, suggesting that bound states at finite separation form at $\kappa \gtrsim \kappa_c$, where $\Lambda \gtrsim |\lambda_{3r}|$. While longer DNS are needed to confirm these predictions, the model, if accurate, indicates that there is a second cross-over value of κ somewhat larger than κ_c , corresponding to $\Lambda = \lambda_2 = |\lambda_{3r}|$. Figure 22 shows that this cross-over value of κ'_c is approximately 0.089. Based on this cross-over value κ'_c (Fig. 22) obtained from the reduced-order model, we speculate that the final state will be a bound state when $\kappa < \kappa'_c$ (e.g., the cases $\kappa = 0.06$ and 0.08 in Fig. 16), while an equispaced state will be reached when $\kappa > \kappa'_c$ (e.g., the case $\kappa = 0.1$ in Fig. 16). We note that the observed repulsion in DNS and in the ordinary differential equation model aligns with the findings in [98] for the generalized Kuramoto-Sivashinsky equation, where an interaction of one oscillatory tail and one monotonic tail was also found to result in repulsion of localized pulses.

B. Collision for $\kappa < \kappa_c$

Next, we compare the reduced model with the DNS results for the chasing, inelastic collision between a single pulse and a two-pulse bound state, shown in Fig. 19(a) at $\kappa = 0.03$ (where $\Lambda = \lambda_1$) in a domain of size $L_x = 80$, leading to the formation of a bound state of three pulses. We again initialize the reduced model with the same initial positions of the proximate maxima as in the DNS. To compare DNS and reduced model results quantitatively, we consider the

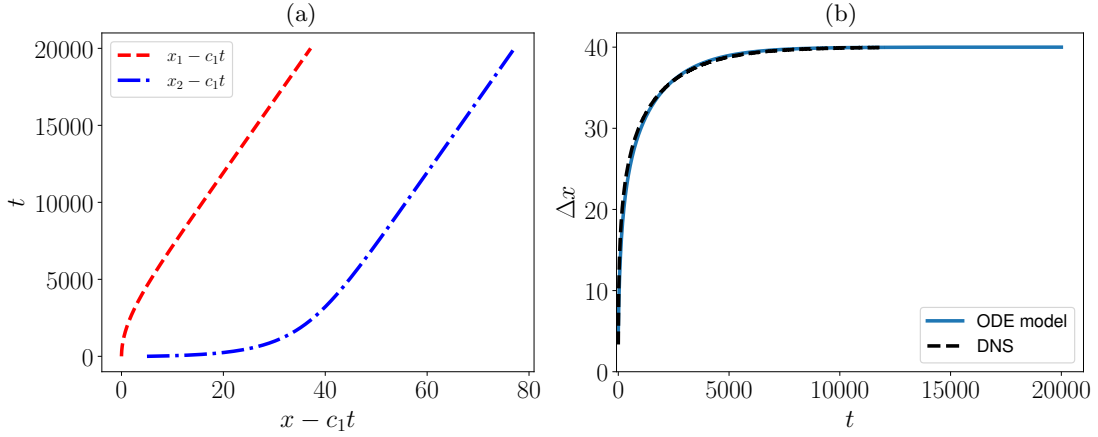


FIG. 20. (a) Trajectories in the comoving frame of two identical interacting pulses, which in the absence of interactions propagate at velocity c_1 , in a domain of size $L_x = 80$ at $\kappa = 0.95$ with spatial eigenvalues $\Lambda = 0.1274$, $\lambda_3 = -1.35 + 2.56i$, computed from the reduced model in Eq. (11) with parameters $g_2 = -g_1 = 0.347$, $\varphi = 0$ estimated by fitting the trajectories to the corresponding DNS data. (b) The separation Δx as a function of time for the two repelling pulses from DNS [see Fig. 17], and from the reduced model. The fact that the two curves overlap indicates that the reduced model accurately captures the dynamics observed in the DNS.

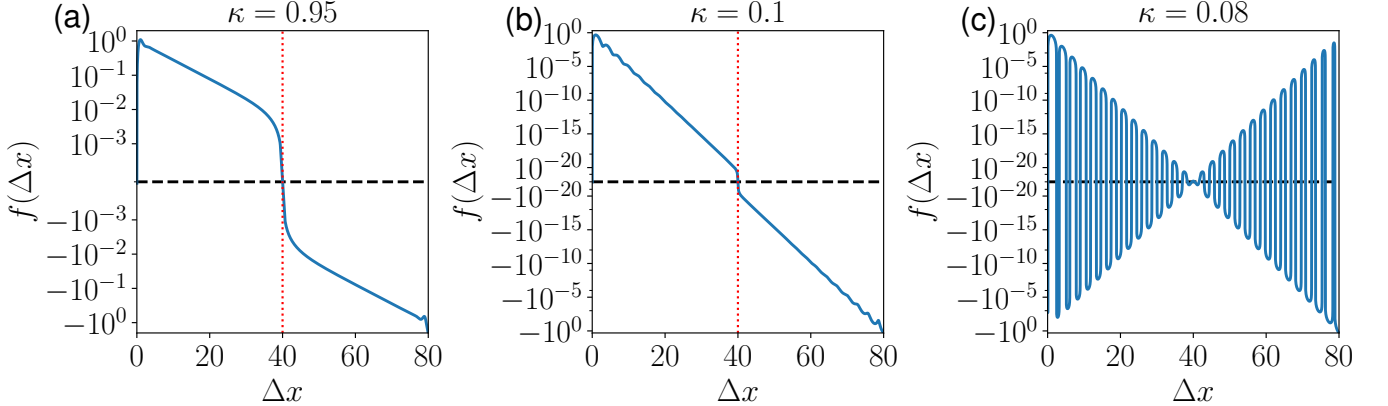


FIG. 21. Residual $f(\Delta x)$ defined in Eq. (12) versus Δx in a domain of size $L_x = 80$ with spatial eigenvalues $\Lambda = 0.1274$, $\lambda_3 = -1.35 + 2.56i$ for $\kappa = 0.95$ [panel (a)], $\Lambda = 1.176$, $\lambda_3 = -1.2848 + 2.20i$ for $\kappa = 0.1$ [panel (b)] and $\Lambda = 1.4090$, $\lambda_3 = -1.2632 + 2.25i$ for $\kappa = 0.08$ [panel (c)]. When $\Lambda > |\text{Re}(\lambda_3)|$, the residual $f(\Delta x)$ only has one root $\Delta x = L_x/2$, indicated by the vertical dashed line in panels (a) and (b), while for $\Lambda < |\text{Re}(\lambda_3)|$, in panel (c), there are many equilibria. In these examples, we assumed that $g_1 = -g_2$ and $\varphi = 0$. The vertical axis is symmetric about zero and logarithmic, with a cutoff at $\pm 10^{-3}$ [panel (a)] and $\pm 10^{-21}$ [panels (b), (c)].

deviation of the relative distance between proximate maxima from free propagation, namely

$$\chi(t) \equiv \Delta x(t) - (c_2 - c_1)t - \Delta x(t=0), \quad (13)$$

where we recall that $\Delta x(t) \equiv |x_2 - x_1|$. When the two structures are located far apart from one another $\chi = 0$, and nonzero values of χ are caused by interactions. Figure 23 shows a comparison between $\chi(t)$ from DNS (black line, noisy due to finite grid resolution) and the reduced model (yellow dashed line). At early times $\chi(t) \approx 0$ since interactions are exponentially weak, leading to effectively free propagation. For reference $\chi = 0$ is indicated by the horizontal grey dashed line at all times. At $t \approx 6000$, deviations from $\chi = 0$ indicate the onset of significant interactions of alternating sign between the two localized structures: first, a small deviation towards negative χ can be seen, signifying attraction, followed by a larger-amplitude positive deviation in χ , indicating repulsion, which is in turn followed by a larger-amplitude, negative deviation in χ , implying renewed attraction. The evolution shown in Fig. 23 closely resembles the results reported for collisions of localized structures in the Swift-Hohenberg equation [79]. The vertical blue dotted line in Fig. 23 indicates the time when the new three-pulse bound state is formed in the collision, after which the relative distance is constant, leading to a linear increase in $\chi(t)$, cf. Eq. (13). Since χ is negative at

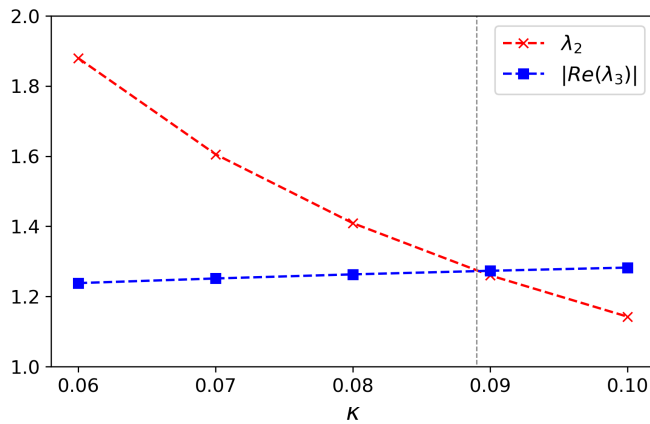


FIG. 22. Leading spatial eigenvalue λ_2 (red crosses interpolated by red dashed line) and $|\text{Re}(\lambda_3)|$ (blue squares interpolated by blue dashed line) as a function of κ , revealing a cross-over point at $\kappa'_c \approx 0.089$, denoted by the vertical grey dashed line. The spatial eigenvalues shown here were computed with c measured for a single pulse in $L_x = 40$.

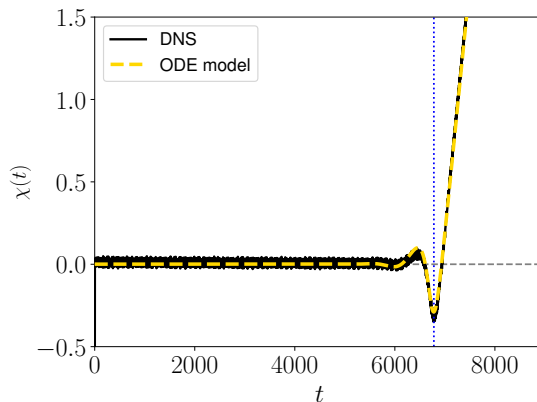


FIG. 23. Compensated distance $\chi(t)$ defined in Eq. (13) versus time from DNS (black line, noisy due to finite grid resolution) at $\kappa = 0.03$ in a domain of size $L_x = 80$ (Fig. 19), and the reduced model (yellow dashed line) with $g_1 = -1.62145867$, $g_2 = 0.18617327$, $\varphi = 1.85636433$, estimated by a fitting procedure with spatial eigenvalues $\Lambda = 1.5884 + 2.2528i$ and $\lambda_3 = -1.5884 + 2.2528i$. The drift velocities are $c_1 = -0.14165$ and $c_2 = -0.14445$. At early times $\chi(t) \approx 0$ since interactions are weak. For reference, $\chi = 0$ is indicated by the horizontal grey dashed line at all times. At $t \approx 6000$, deviations from $\chi = 0$ indicate the onset of significant interactions of alternating sign between the two localized structures. The vertical blue dotted line indicates the time when the new three-pulse bound state is formed in the collision, after which the relative distance remains constant, leading to a linear increase in $\chi(t)$, cf. Eq. (13).

that time, the collision is effectively attractive in the language proposed in [79]: the formation of the new three-pulse bound state occurs more quickly due to the alternating attractive/repulsive interactions, increasing in strength as the two structures approach each other, than it would by free propagation. Finally, we note that the reduced model can be simplified in this case: the effect of the finite domain size is negligible, since at all times the proximate maxima are much closer to each other than $L_x/2$, and therefore the terms involving $L_x - \Delta x$ in Eq. (11), which represent the interaction with periodic copies, are exponentially suppressed, a conclusion we have verified explicitly (not shown).

The successful quantitative description of the evolution of localized solutions of the system of partial differential equations in Eq. (4), including repulsion and inelastic collisions, by the reduced system of ordinary differential equations in Eq. (11) is indicative of the fact that the interactions between the localized states are to a large extent particlelike, with a nontrivial interaction potential determined by the linearized problem in Eq. (8).

VII. DISCUSSION AND CONCLUSION

In this work, we have investigated the dynamics of traveling spatially localized convective structures (‘traveling convectons’) in an inclined porous layer heated from below. The drift of the convectons, observed here for the first time in a porous medium, is a result of the asymmetry in the top and bottom temperature boundary conditions. For a fixed inclination angle and a fixed Rayleigh number, we conducted extensive DNS (over 300 individual simulations) for different values of the symmetry-breaking parameter κ , related to the Biot number, and different horizontal domain sizes L_x . In DNS with fixed domain size and varying κ , stable, traveling n -pulse states are typically observed in the weak symmetry-breaking regime ($\kappa \lesssim 0.1$). However, in sufficiently small domains n -pulse traveling convectons become unstable as κ increases towards $\kappa = 1$ (strong symmetry breaking). For traveling states consisting of more than one pulse, spatially localized structures can either form a bound state at a small separation or be evenly spread out across the finite computational domain. The drift velocity c of traveling convectons is sensitive to κ (as well as the domain size), exhibiting nontrivial, generically nonlinear relationships $c(\kappa)$. In small domains, the drift velocity c was found to be positive (indicating an upslope travel direction) and monotonically increasing with κ , while in larger domains c is sign-indefinite for localized structures consisting of a few pulses only. DNS with fixed κ and increasing domain size revealed a strong impact of the domain size, which can be attributed to interactions between image structures in adjacent periodic domains. With strong symmetry breaking, multi-pulse localized structures can either decay directly to the conduction state or transition into traveling states with fewer pulses (partial annihilation).

To investigate the long-range interactions between localized structures mediated by their small-amplitude tails, we studied the spatial eigenvalues responsible for the tail profiles. We showed that the spatial eigenvalues which we computed numerically successfully predict the spatial growth rate and wave number of the leading and trailing tails of traveling localized structures in DNS, with accuracy that increases with increasing size of the computational domain. Moreover, the dominant spatial eigenvalue associated with the upslope tail (with a negative real part), which may be leading or trailing depending on the sign of c , remains complex for all parameter values, indicating that the upslope tail is always oscillatory, at least in the parameter regime analyzed here. The dominant spatial eigenvalue associated with the downslope tail (with a positive real part), which can likewise be leading or trailing, shows a competition between a pair of complex eigenvalues and a real eigenvalue, resulting in a transition from an oscillatory tail at small κ to a monotonic tail at large κ . The spatial eigenvalues predict a critical threshold value $\kappa_c \approx 0.059$ for this transition in broad agreement with DNS observations.

The discovery of this transition in the tail profiles sheds light on the interactions between localized structures observed in our DNS. We investigated the long-time dynamics of the interaction between localized pulses by measuring their spatial separation as a function of time. The results suggest that at $\kappa \leq 0.04$, which is in the parameter regime where tails are purely oscillatory, separation converges to a value much less than the largest possible separation in the domain, indicating the existence of bound states in a domain of size $L_x = 40$. This result aligns with the fact that interaction between oscillatory tails of localized structures is usually associated with the formation of bound states. We emphasize that the bound states are by no means unique: we expect a multiplicity of such states differing only in the interpulse separation. This separation is in turn determined by the locking of adjacent pulse tails. However, these states are not observed here and may be unstable.

On the other hand, for $\kappa > \kappa_c$ our DNS results for a traveling two-pulse structure confirm that for $\kappa > 0.2$ adjacent pulses repel one another, resulting ultimately in the largest possible separation in the domain ($\Delta x = 20$). The repulsive interaction resulting from the change in the tail profile for $\kappa > \kappa_c$ is not fully investigated numerically in this work. This is because, on the one hand, the interaction decreases rapidly with the separation between the two structures, and on the other hand, the drift velocity also decreases significantly in the weakly broken symmetry regime (i.e. $\kappa \lesssim 0.1$). As a result, very long simulation times are required to verify whether the final traveling localized structures are evolving towards a bound state or an equispaced state when the domain is large. So far, we have yet to observe traveling equispaced states (or traveling bound states) in simulations with $0.04 < \kappa \leq 0.2$ in a $L_x = 40$ domain. For the same reason, in a $L_x = 80$ domain, we are able to verify that pulses become strictly equispaced only for $\kappa \geq 0.95$. Complementing these DNS results obtained at the expense of a significant amount of computation time, we adapted a reduced-order model from [79] and showed that it also accurately reproduces the interactions between localized structures in the present model, including pulse repulsion (for $\kappa \gg \kappa_c$) and the inelastic collision of bound states traveling at different velocities (for $\kappa < \kappa_c$). The reduced complexity of this model has provided significant insight into the dynamics, suggesting the existence of a second transition value of κ , with $\kappa = \kappa'_c > \kappa_c$. More precisely, the reduced model suggests that in the presence of one oscillatory tail and one monotonic tail and $\kappa > \kappa'_c$, the resulting repulsion of identical pulses always leads to an equispaced configuration at late times, while in the weakly supercritical regime $\kappa_c < \kappa < \kappa'_c$ the reduced model indicates that bound states with a smaller separation than in the equispaced configuration may continue to form, although longer DNS are needed to test this prediction. Nevertheless, the good agreement between the reduced model and the solutions of the full fluid equations indicates that the interactions of localized convective structures are to a great extent particle-like.

A key aspect of this work was to gain insight into the effects of breaking a reflection symmetry, here the symmetry \mathcal{R} , and into the ensuing dynamics, but in other systems rotation [118] or throughflow [119] play a similar role. In systems with periodic boundary conditions a spatially periodic state with a nonzero wave number generically begins to drift when the symmetry is broken, either externally as here or through spontaneous symmetry breaking, i.e., at a parity-breaking bifurcation. However, large domains can support multiple traveling states with distinct wave numbers and velocities, and one expects to find transitions between them as parameters are varied, cf. [120]. These transitions may be hysteretic or continuous, but in each case occur via a branch of two-frequency states connecting the primary states [121]. These statements apply equally to spatially localized states. We conjecture that the Newton's cradle solutions (Figs. 14 and 15) are examples of stable two-frequency states of this type, connecting branches of single-frequency traveling states at either end of their existence interval. We mention that the fact that the two- and four-pulse traveling states are simultaneously stable provides evidence for a hysteretic transition between them. Evidently, numerical continuation techniques would be helpful to resolve some of these conjectures. We mention that disconnected asymmetric localized traveling states may be present even in systems with reflection symmetry, and accessed - as here - via a finite amplitude perturbation only [77].

It is evident that many aspects of the present problem remain to be explored. For weakly broken midplane reflection symmetry, the drift speed of localized structures can in many cases be predicted using asymptotic techniques, see e.g. [79], and adapting these techniques to the present system, where the symmetry-breaking parameter κ only appears in the boundary conditions, will be an important next step. Furthermore, while the present work largely relies on DNS, numerical continuation and a stability analysis of spatially localized structures in this system would provide crucial additional insights. This would in particular help clarify to what extent this system follows typical bifurcation structures of spatially localized structures such as homoclinic snaking found in the Swift-Hohenberg equation [40, 96] and how this is impacted by the broken reflection symmetry \mathcal{R} . Finally, this study focused exclusively on the case $Ra = 100$, $\phi = 35^\circ$, and other choices of parameters, as well as a three-dimensional geometry, remain of interest. The current 2D results can be viewed as describing transverse rolls where the roll axes are orthogonal to the shear flow arising from buoyancy. It is well known, however, that in 3D certain parameter regimes favor longitudinal rolls [31, 37], where the roll axes are aligned with the shear flow direction. As a result, it is reasonable to expect much richer flow physics will appear in 3D, much as occurs in 3D inclined Rayleigh-Bénard convection [33, 34].

ACKNOWLEDGMENTS

This work was supported by the National Science Foundation (Grants DMS-2009563, DMS-2308337, DMS-2308338 and OCE-2023541) and by Deutsche Forschungsgemeinschaft (DFG Projektnummer: 522026592). The computational resources for this project were provided by the NSF ACCESS program (project number: PHY230056), allowing us to utilize the Advanced Research Computing at the Johns Hopkins (ARCH) core facility (rockfish.jhu.edu), which is supported by the National Science Foundation under grant number OAC 1920103, and the Purdue Anvil CPU cluster [122]. C.L. acknowledges the support from UConn Research Excellence Program and UConn Quantum Innovation Seed Grants.

-
- [1] A. Riaz, M. Hesse, H. A. Tchelepi, and F. M. Orr, Onset of convection in a gravitationally unstable diffusive boundary layer in porous media, *J. Fluid Mech.* **548**, 87 (2006).
 - [2] B. Wen, D. Akhbari, L. Zhang, and M. A. Hesse, Convective carbon dioxide dissolution in a closed porous medium at low pressure, *J. Fluid Mech.* **854**, 56 (2018).
 - [3] J. H. George, R. D. Gunn, and B. Straughan, Patterned ground formation and penetrative convection in porous media, *Geophys. & Astrophys. Fluid Dyn.* **46**, 135 (1989).
 - [4] J. Lasser, J. M. Nield, M. Ernst, V. Karius, G. F. S. Wiggs, M. R. Threadgold, C. Beaume, and L. Goehring, Salt polygons and porous media convection, *Phys. Rev. X* **13**, 011025 (2023).
 - [5] W.-J. Chang and D.-F. Yang, Natural convection for the melting of ice in porous media in a rectangular enclosure, *Int. J. Heat Mass Transf.* **39**, 2333 (1996).
 - [6] A. V. Shenoy, Non-Newtonian fluid heat transfer in porous media, in *Advances in Heat Transfer*, Vol. 24 (Elsevier, 1994) pp. 101–190.
 - [7] C. W. Horton and F. T. Rogers Jr, Convection currents in a porous medium, *J. Appl. Phys.* **16**, 367 (1945).
 - [8] F. T. Rogers Jr, Convection currents in porous media. V. Variational form of the theory, *J. Appl. Phys.* **24**, 877 (1953).
 - [9] M. Mamou, P. Vasseur, and E. Bilgen, Double-diffusive convection instability in a vertical porous enclosure, *J. Fluid Mech.* **368**, 263 (1998).
 - [10] M. Mamou and P. Vasseur, Thermosolutal bifurcation phenomena in porous enclosures subject to vertical temperature and concentration gradients, *J. Fluid Mech.* **395**, 61 (1999).

- [11] A. Mahidjiba, M. Mamou, and P. Vasseur, Onset of double-diffusive convection in a rectangular porous cavity subject to mixed boundary conditions, *Int. J. Heat Mass Transfer* **43**, 1505 (2000).
- [12] C. Liu and E. Knobloch, Single-mode solutions for convection and double-diffusive convection in porous media, *Fluids* **7**, 373 (2022).
- [13] J. Otero, L. A. Dontcheva, H. Johnston, R. A. Worthing, A. Kurganov, G. Petrova, and C. R. Doering, High-Rayleigh-number convection in a fluid-saturated porous layer, *J. Fluid Mech.* **500**, 263 (2004).
- [14] D. R. Hewitt, J. A. Neufeld, and J. R. Lister, Ultimate regime of high Rayleigh number convection in a porous medium, *Phys. Rev. Lett.* **108**, 224503 (2012).
- [15] D. R. Hewitt, J. A. Neufeld, and J. R. Lister, High Rayleigh number convection in a three-dimensional porous medium, *J. Fluid Mech.* **748**, 879 (2014).
- [16] B. Wen, L. T. Corson, and G. P. Chini, Structure and stability of steady porous medium convection at large Rayleigh number, *J. Fluid Mech.* **772**, 197 (2015).
- [17] S. Pirozzoli, M. De Paoli, F. Zonta, and A. Soldati, Towards the ultimate regime in Rayleigh–Darcy convection, *J. Fluid Mech.* **911**, R4 (2021).
- [18] X. Zhu, Y. Fu, and M. De Paoli, Transport scaling in porous media convection, *J. Fluid Mech.* **991**, A4 (2024).
- [19] D. A. Nield and A. V. Kuznetsov, An historical and topical note on convection in porous media, *J. Heat Transfer* **135**, 061201 (2013).
- [20] H. E. Huppert and J. A. Neufeld, The fluid mechanics of carbon dioxide sequestration, *Annu. Rev. Fluid Mech.* **46**, 255 (2014).
- [21] D. R. Hewitt, Vigorous convection in porous media, *Proc. R. Soc. Lond. A* **476**, 20200111 (2020).
- [22] M. De Paoli, Convective mixing in porous media: a review of Darcy, pore-scale and Hele-Shaw studies, *Eur. Phys. J. E* **46**, 129 (2023).
- [23] D. A. Nield and A. Bejan, *Convection in Porous Media*, Vol. 3 (Springer, 2006).
- [24] L. Storesletten, Effects of anisotropy on convective flow through porous media, in *Transport Phenomena in Porous Media*, edited by D. B. Ingham and I. POP (Pergamon, Oxford, 1998) pp. 261–283.
- [25] J. Ennis-King, I. Preston, and L. Paterson, Onset of convection in anisotropic porous media subject to a rapid change in boundary conditions, *Phys. Fluids* **17**, 084107 (2005).
- [26] M. De Paoli, F. Zonta, and A. Soldati, Dissolution in anisotropic porous media: Modelling convection regimes from onset to shutdown, *Phys. Fluids* **29**, 026601 (2017).
- [27] O. V. Trevisan and A. Bejan, Mass and heat transfer by high Rayleigh number convection in a porous medium heated from below, *Int. J. Heat Mass Transfer* **30**, 2341 (1987).
- [28] N. D. Rosenberg and F. J. Spera, Thermohaline convection in a porous medium heated from below, *Int. J. Heat Mass Transfer* **35**, 1261 (1992).
- [29] J. A. Neufeld, M. A. Hesse, A. Riaz, M. A. Hallworth, H. A. Tchelepi, and H. E. Huppert, Convective dissolution of carbon dioxide in saline aquifers, *Geophys. Res. Lett.* **37**, L22404 (2010).
- [30] P. Vadasz, Instability and convection in rotating porous media: A review, *Fluids* **4**, 147 (2019).
- [31] B. Wen and G. P. Chini, Inclined porous medium convection at large Rayleigh number, *J. Fluid Mech.* **837**, 670 (2018).
- [32] B. Wen and G. P. Chini, On moderate-Rayleigh-number convection in an inclined porous layer, *Fluids* **4**, 101 (2019).
- [33] F. Reetz and T. M. Schneider, Invariant states in inclined layer convection. Part 1. Temporal transitions along dynamical connections between invariant states, *J. Fluid Mech.* **898**, A22 (2020).
- [34] F. Reetz, P. Subramanian, and T. M. Schneider, Invariant states in inclined layer convection. Part 2. Bifurcations and connections between branches of invariant states, *J. Fluid Mech.* **898**, A23 (2020).
- [35] J. Singh, Longitudinal and transverse modes of temperature-modulated inclined layer convection, *Phys. Rev. E* **107**, 045104 (2023).
- [36] S. A. Bories and M. A. Combarous, Natural convection in a sloping porous layer, *J. Fluid Mech.* **57**, 63 (1973).
- [37] J. P. Caltagirone and S. Bories, Solutions and stability criteria of natural convective flow in an inclined porous layer, *J. Fluid Mech.* **155**, 267 (1985).
- [38] D. A. S. Rees and A. P. Bassom, The onset of Darcy–Bénard convection in an inclined layer heated from below, *Acta Mech.* **144**, 103 (2000).
- [39] H.-G. Purwins, H. U. Bödeker, and S. Amiranashvili, Dissipative solitons, *Adv. Phys.* **59**, 485 (2010).
- [40] E. Knobloch, Spatial localization in dissipative systems, *Annu. Rev. Condens. Matter Phys.* **6**, 325 (2015).
- [41] J. Burke and E. Knobloch, Localized states in the generalized Swift-Hohenberg equation, *Phys. Rev. E* **73**, 056211 (2006).
- [42] J. Burke, S. M. Houghton, and E. Knobloch, Swift-Hohenberg equation with broken reflection symmetry, *Phys. Rev. E* **80**, 036202 (2009).
- [43] S. M. Houghton and E. Knobloch, Swift-Hohenberg equation with broken cubic-quintic nonlinearity, *Phys. Rev. E* **84**, 016204 (2011).
- [44] T. M. Schneider, J. F. Gibson, and J. Burke, Snakes and ladders: localized solutions of plane Couette flow, *Phys. Rev. Lett.* **104**, 104501 (2010).
- [45] M. D. Graham and D. Floryan, Exact coherent states and the nonlinear dynamics of wall-bounded turbulent flows, *Annu. Rev. Fluid Mech.* **53**, 227 (2021).
- [46] G. Kawahara, M. Uhlmann, and L. Van Veen, The significance of simple invariant solutions in turbulent flows, *Annu. Rev. Fluid Mech.* **44**, 203 (2012).
- [47] P. Kolodner, C. M. Surko, and H. Williams, Dynamics of traveling waves near the onset of convection in binary fluid mixtures, *Physica D* **37**, 319 (1989).

- [48] V. Steinberg, J. Fineberg, E. Moses, and I. Rehberg, Pattern selection and transition to turbulence in propagating waves, *Physica D* **37**, 359 (1989).
- [49] P. Kolodner, Drift, shape, and intrinsic destabilization of pulses of traveling-wave convection, *Phys. Rev. A* **44**, 6448 (1991).
- [50] W. Barten, M. Lücke, and M. Kamps, Localized traveling-wave convection in binary-fluid mixtures, *Phys. Rev. Lett.* **66**, 2621 (1991).
- [51] W. Barten, M. Lücke, M. Kamps, and R. Schmitz, Convection in binary fluid mixtures. II. Localized traveling waves, *Phys. Rev. E* **51**, 5662 (1995).
- [52] D. Jung and M. Lücke, Traveling wave fronts and localized traveling wave convection in binary fluid mixtures, *Phys. Rev. E* **72**, 026307 (2005).
- [53] T. Watanabe, M. Iima, and Y. Nishiura, A skeleton of collision dynamics: hierarchical network structure among even-symmetric steady pulses in binary fluid convection, *SIAM J. Appl. Dyn. Syst.* **15**, 789 (2016).
- [54] P. Kolodner, Collisions between pulses of traveling-wave convection, *Phys. Rev. A* **44**, 6466 (1991).
- [55] A. V. Taraut, B. L. Smorodin, and M. Lücke, Collisions of localized convection structures in binary fluid mixtures, *New J. Phys.* **14**, 093055 (2012).
- [56] M. Iima and Y. Nishiura, Collision of localized traveling-wave convection cells in binary fluid, in *Mathematical Sciences and Applications*, Vol. 22 (Gakkotosho, 2005) pp. 289–303.
- [57] S. Blanchflower, Magnetohydrodynamic convectons, *Phys. Lett. A* **261**, 74 (1999).
- [58] S. Blanchflower and N. Weiss, Three-dimensional magnetohydrodynamic convectons, *Phys. Lett. A* **294**, 297 (2002).
- [59] J. H. P. Dawes, Localized convection cells in the presence of a vertical magnetic field, *J. Fluid Mech.* **570**, 385 (2007).
- [60] D. L. Jacono, A. Bergeon, and E. Knobloch, Magnetohydrodynamic convectons, *J. Fluid Mech.* **687**, 595 (2011).
- [61] O. Batiste and E. Knobloch, Simulations of localized states of stationary convection in $\text{He}^3\text{-He}^4$ mixtures, *Phys. Rev. Lett.* **95**, 244501 (2005).
- [62] O. Batiste, E. Knobloch, A. Alonso, and I. Mercader, Spatially localized binary-fluid convection, *J. Fluid Mech.* **560**, 149 (2006).
- [63] I. Mercader, A. Alonso, and O. Batiste, Spatiotemporal dynamics near the onset of convection for binary mixtures in cylindrical containers, *Phys. Rev. E* **77**, 036313 (2008).
- [64] D. Lo Jacono, A. Bergeon, and E. Knobloch, Spatially localized binary fluid convection in a porous medium, *Phys. Fluids* **22**, 073601 (2010).
- [65] I. Mercader, O. Batiste, A. Alonso, and E. Knobloch, Dissipative solitons in binary fluid convection, *Discrete Contin. Dyn. Syst. Ser. S* **4**, 1213 (2011).
- [66] I. Mercader, O. Batiste, A. Alonso, and E. Knobloch, Convectons, anticonvectons and multiconvectons in binary fluid convection, *J. Fluid Mech.* **667**, 586 (2011).
- [67] I. Mercader, O. Batiste, A. Alonso, and E. Knobloch, Travelling convectons in binary fluid convection, *J. Fluid Mech.* **722**, 240 (2013).
- [68] D. L. Jacono, A. Bergeon, and E. Knobloch, Three-dimensional spatially localized binary-fluid convection in a porous medium, *J. Fluid Mech.* **730**, R2 (2013).
- [69] D. L. Jacono, A. Bergeon, and E. Knobloch, Complex convective structures in three-dimensional binary fluid convection in a porous medium, *Fluid Dyn. Res.* **49**, 061402 (2017).
- [70] P. Assemat, A. Bergeon, and E. Knobloch, Spatially localized states in Marangoni convection in binary mixtures, *Fluid Dyn. Res.* **40**, 852 (2008).
- [71] C. Beaume, A. Bergeon, H.-C. Kao, and E. Knobloch, Convectons in a rotating fluid layer, *J. Fluid Mech.* **717**, 417 (2013).
- [72] C. Beaume, A. Bergeon, and E. Knobloch, Homoclinic snaking of localized states in doubly diffusive convection, *Phys. Fluids* **23**, 094102 (2011).
- [73] C. Beaume, A. Bergeon, and E. Knobloch, Convectons and secondary snaking in three-dimensional natural doubly diffusive convection, *Phys. Fluids* **25**, 024105 (2013).
- [74] C. Beaume, A. Bergeon, and E. Knobloch, Three-dimensional doubly diffusive convectons: instability and transition to complex dynamics, *J. Fluid Mech.* **840**, 74 (2018).
- [75] J. Tumelty, C. Beaume, and A. M. Rucklidge, Toward convectons in the supercritical regime: Homoclinic snaking in natural doubly diffusive convection, *SIAM J. Appl. Dyn. Syst.* **22**, 1710 (2023).
- [76] P. Schütz, M. Bode, and V. V. Gafichuk, Transition from stationary to traveling localized patterns in a two-dimensional reaction-diffusion system, *Phys. Rev. E* **52**, 4465 (1995).
- [77] D. Lo Jacono, A. Bergeon, and E. Knobloch, Localized traveling pulses in natural doubly diffusive convection, *Phys. Rev. Fluids* **2**, 093501 (2017).
- [78] L. Ophaus, S. V. Gurevich, and U. Thiele, Resting and traveling localized states in an active phase-field-crystal model, *Phys. Rev. E* **98**, 022608 (2018).
- [79] M. Raja, A. van Kan, B. Foster, and E. Knobloch, Collisions of localized patterns in a nonvariational Swift-Hohenberg equation, *Phys. Rev. E* **107**, 064214 (2023).
- [80] K. J. Burns, G. M. Vasil, J. S. Oishi, D. Lecoanet, and B. P. Brown, Dedalus: A flexible framework for numerical simulations with spectral methods, *Phys. Rev. Res.* **2**, 023068 (2020).
- [81] U. M. Ascher, S. J. Ruuth, and R. J. Spiteri, Implicit-explicit Runge-Kutta methods for time-dependent partial differential equations, *Appl. Numer. Math.* **25**, 151 (1997).
- [82] M. Or-Guil, I. G. Kevrekidis, and M. Bär, Stable bound states of pulses in an excitable medium, *Physica D* **135**, 154

- (2000).
- [83] A. Yochelis, E. Knobloch, Y. Xie, Z. Qu, and A. Garfinkel, Generation of finite wave trains in excitable media, *Europhys. Lett.* **83**, 64005 (2008).
 - [84] A. Yochelis, E. Knobloch, and M. H. Köpf, Origin of finite pulse trains: Homoclinic snaking in excitable media, *Phys. Rev. E* **91**, 032924 (2015).
 - [85] A. Bergeon and E. Knobloch, Dynamics and formation of localized states in flowing thin films: Bound states of solitary waves, in *J. Phys. Conf. Ser.*, Vol. 216 (IOP Publishing, 2010) p. 012001.
 - [86] K. Kirchgässner, Wave-solutions of reversible systems and applications, *J. Differ. Equ.* **45**, 113 (1982).
 - [87] M. Haragus and G. Iooss, *Local Bifurcations, Center Manifolds, and Normal Forms in Infinite-dimensional Dynamical Systems*, Vol. 3 (Springer, 2011).
 - [88] J. Burke, A. Yochelis, and E. Knobloch, Classification of spatially localized oscillations in periodically forced dissipative systems, *SIAM J. Appl. Dyn. Syst.* **7**, 651 (2008).
 - [89] J. Burke and J. H. P. Dawes, Localized states in an extended Swift–Hohenberg equation, *SIAM J. Appl. Dyn. Syst.* **11**, 261 (2012).
 - [90] P. Parra-Rivas, D. Gomila, L. Gelens, and E. Knobloch, Bifurcation structure of localized states in the Lugiato-Lefever equation with anomalous dispersion, *Phys. Rev. E* **97**, 042204 (2018).
 - [91] E. Knobloch and A. Yochelis, Stationary peaks in a multivariable reaction–diffusion system: foliated snaking due to subcritical Turing instability, *IMA J. Appl. Math.* **86**, 1066 (2021).
 - [92] P. Parra-Rivas, E. Knobloch, L. Gelens, and D. Gomila, Origin, bifurcation structure and stability of localized states in Kerr dispersive optical cavities, *IMA J. Appl. Math.* **86**, 856 (2021).
 - [93] N. Verschueren and A. R. Champneys, Dissecting the snake: transition from localized patterns to spike solutions, *Physica D* **419**, 132858 (2021).
 - [94] T. Frohoff-Hülsmann and U. Thiele, Localized states in coupled Cahn–Hilliard equations, *IMA J. Appl. Math.* **86**, 924 (2021).
 - [95] F. Al Saadi, A. Champneys, and N. Verschueren, Localized patterns and semi-strong interaction, a unifying framework for reaction–diffusion systems, *IMA J. Appl. Math.* **86**, 1031 (2021).
 - [96] J. Burke and E. Knobloch, Localized states in the generalized Swift-Hohenberg equation, *Phys. Rev. E* **73**, 056211 (2006).
 - [97] J. A. Weideman and S. C. Reddy, A MATLAB differentiation matrix suite, *ACM Trans. Math. Softw.* **26**, 465 (2000).
 - [98] T. Kawahara and S. Toh, Pulse interactions in an unstable dissipative-dispersive nonlinear system, *Phys. Fluids* **31**, 2103 (1988).
 - [99] S. Kalliadasis and U. Thiele, *Thin films of soft matter*, CISM Courses and Lectures, Vol. 490 (Springer, 2007).
 - [100] K. A. Gorshkov and L. A. Ostrovsky, Interactions of solitons in nonintegrable systems: direct perturbation method and applications, *Physica D* **3**, 428 (1981).
 - [101] I. S. Aranson, K. A. Gorshkov, A. S. Lomov, and M. I. Rabinovich, Stable particle-like solutions of multidimensional nonlinear fields, *Physica D* **43**, 435 (1990).
 - [102] A. G. Vladimirov, J. M. McSloy, D. V. Skryabin, and W. J. Firth, Two-dimensional clusters of solitary structures in driven optical cavities, *Phys. Rev. E* **65**, 046606 (2002).
 - [103] M. Tlidi, A. G. Vladimirov, and P. Mandel, Interaction and stability of periodic and localized structures in optical bistable systems, *IEEE J. Quantum Electron.* **39**, 216 (2003).
 - [104] M. Tlidi, R. Lefever, and A. Vladimirov, On vegetation clustering, localized bare soil spots and fairy circles, in *Dissipative Solitons: From Optics to Biology and Medicine* (Springer, 2008) pp. 1–22.
 - [105] M. G. Clerc, S. Coulibaly, and D. Laroze, Interaction law of 2D localized precession states, *Europhys. Lett.* **90**, 38005 (2010).
 - [106] J. Burke and E. Knobloch, Multipulse states in the Swift-Hohenberg equation, *Discrete and continuous dynamical systems - Conference Publications* **2009**, 109 (2009).
 - [107] S.-I. Ei and T. Ohta, Equation of motion for interacting pulses, *Phys. Rev. E* **50**, 4672 (1994).
 - [108] T. Ohta, Pulse dynamics in a reaction–diffusion system, *Physica D* **151**, 61 (2001).
 - [109] E. Berríos-Caro, M. G. Clerc, D. Escaff, C. Sandivari, and M. Tlidi, On the repulsive interaction between localised vegetation patches in scarce environments, *Sci. Rep.* **10**, 5740 (2020).
 - [110] B. Eiermann, T. Anker, M. Albiez, M. Taglieber, P. Treutlein, K.-P. Marzlin, and M. K. Oberthaler, Bright Bose-Einstein gap solitons of atoms with repulsive interaction, *Phys. Rev. Lett.* **92**, 230401 (2004).
 - [111] T. Watanabe, M. Iima, and Y. Nishiura, Spontaneous formation of travelling localized structures and their asymptotic behaviour in binary fluid convection, *J. Fluid Mech.* **712**, 219 (2012).
 - [112] Y.-P. Ma and E. Knobloch, Depinning, front motion, and phase slips, *Chaos* **22**, 033101 (2012).
 - [113] P. Couillet, C. Elphick, and D. Repaux, Nature of spatial chaos, *Phys. Rev. Lett.* **58**, 431 (1987).
 - [114] C. Elphick, G. R. Ierley, O. Regev, and E. A. Spiegel, Interacting localized structures with Galilean invariance, *Phys. Rev. A* **44**, 1110 (1991).
 - [115] N. J. Balmforth, G. R. Ierley, and E. A. Spiegel, Chaotic pulse trains, *SIAM J. Appl. Math.* **54**, 1291 (1994).
 - [116] G. Kozyreff and L. Gelens, Cavity solitons and localized patterns in a finite-size optical cavity, *Phys. Rev. A* **84**, 023819 (2011).
 - [117] Y. Nishiura and T. Watanabe, Traveling pulses with oscillatory tails, figure-eight-like stack of isolas, and dynamics in heterogeneous media, *Physica D* **440**, 133448 (2022).
 - [118] R. E. Ecke, F. Zhong, and E. Knobloch, Hopf bifurcation with broken reflection symmetry in rotating Rayleigh-Bénard convection, *Europhys. Lett.* **19**, 177 (1992).

- [119] P. Büchel and M. Lücke, Influence of through flow on binary fluid convection, *Phys. Rev. E* **61**, 3793 (2000).
- [120] E. Knobloch and J. Guckenheimer, Convective transitions induced by a varying aspect ratio, *Phys. Rev. A* **27**, 408 (1983).
- [121] E. Knobloch, Bifurcations in rotating systems, in *Lectures on Solar and Planetary Dynamos*, Publications of the Newton Institute, edited by M. R. E. Proctor and A. D. Gilbert (Cambridge University Press, 1994) pp. 331–372.
- [122] X. C. Song, P. Smith, R. Kalyanam, X. Zhu, E. Adams, K. Colby, P. Finnegan, E. Gough, E. Hillery, R. Irvine, A. Maji, and J. St. John, Anvil-system architecture and experiences from deployment and early user operations, in *Practice and Experience in Advanced Research Computing* (2022) pp. 1–9.